Rapid Multi-Mode Trapped-Ion Laser Cooling in a Phase-Stable Standing Wave

Zhenzhong Xing,[1,*,†] Hamim Mahmud Rivy,[1,*,‡] Vighnesh Natarajan,[1] Aditya Milind Kolhatkar,[1] Gillenhaal Beck,[2] and Karan K. Mehta[1,§]

[1]*School of Electrical and Computer Engineering, Cornell University, Ithaca, New York 14853, USA*
[2]*Institute for Quantum Electronics, ETH Zurich, 8093 Zurich, Switzerland*

(Received 12 March 2026; revised 12 September 2026; accepted 15 October 2026; published 9 November 2026)

Laser cooling is fundamental to quantum computing and metrology using atomic systems. Precise control often requires cooling atoms' motional degrees of freedom to the quantum ground state, imposing operation time and architectural limitations particularly in large-scale systems. Here we demonstrate how the integrated optical control of interest for scaling trapped-ion systems additionally enables laser cooling that bypasses limitations of conventional schemes. Leveraging multi-channel integrated delivery of ultraviolet to infrared wavelengths for calcium ion control including in passively phase-stable ultraviolet standing waves (SWs), we experimentally verify a long-standing prediction by Cirac *et al.*, realizing Doppler cooling to below the conventional Doppler limit at a SW node. We also present the first realization of ground-state cooling via electromagnetically induced transparency (EIT) using a "probe" beam delivered as a SW with atoms positioned at a node, predicted to enable multi-mode sub-recoil-limit laser cooling. We demonstrate cooling of motional modes spanning an approximately 5 MHz bandwidth from the Doppler temperature to near the ground state within 150 μs, reaching $\bar{n} \approx 0.05$ phonon number occupancies for the target mode. Direct evaluation against the comparable running-wave (RW) scheme shows the SW implementation's simultaneous advantage in cooling rate, motional mode bandwidth, and final phonon number, as previously theoretically predicted. Our work leverages capabilities enabled by integrated optical delivery to demonstrate fast cooling of multiple modes to the quantum ground state, and more broadly how scalable approaches to optical control can enable enhancements in fundamental atomic functionalities.

DOI: 10.1103/5btm-vwgy

I. INTRODUCTION

Trapped-ion quantum computing (QC) [1] and metrology rely on laser cooling for precise coherent control. State-of-the-art QC systems based for example on quantum charge-coupled device schemes [2–4] employ repeated ground-state laser cooling to mitigate unintended excitation following transport and ion crystal reconfiguration operations [5–7] and to mitigate inevitable heating during operation [8]. In many QC architectures, total runtime can be dominated by transport and repeated ground-state cooling [4,9], often implemented via resolved sideband cooling of individual modes [10]. Cooling times required can be severe given that high-fidelity laser-based quantum logic often requires low phonon number occupancies for multiple motional modes spread over multiple MHz bandwidths [11]. Polarization-gradient [12,13] and electromagnetically induced transparency (EIT) cooling [14,15] offer routes to sub-Doppler cooling for multiple modes simultaneously, but are often limited to higher phonon numbers than those achievable with sideband cooling.

Optical delivery leveraging waveguide photonics integrated in ion traps [16–19] stands to address challenges related to scaling and parallelizing trapped-ion optical control [20–22]. Beyond scaling, integrated addressing brings passive phase and amplitude stability which enables practical delivery of spatially structured driving fields, and thereby tailoring of laser-ion interactions in ways that can alleviate limitations on basic physical operations. This has been proposed and explored for example via delivery of phase-stable standing waves (SWs) [23–26] and polarization gradients [27,28].

Previous work has examined laser cooling in SWs theoretically, both for Doppler cooling [29] and for schemes capable of reaching the quantum ground state based on electromagnetically induced transparency (EIT) [14,15].

*These authors contributed equally to this work.
†Contact author: zx296@cornell.edu
‡Contact author: hr296@cornell.edu
§Contact author: karanmehta@cornell.edu

Published by the American Physical Society under the terms of the Creative Commons Attribution 4.0 International license. Further distribution of this work must maintain attribution to the author(s) and the published article's title, journal citation, and DOI.

Due to the suppression of coherent carrier coupling for atoms located at SW nulls [30] and the associated photon scattering undesired for laser cooling, theoretical treatments have predicted modest advantages in cooling speed and phonon number limits for Doppler cooling. For ground-state EIT cooling, use of a SW "probe" or "cooling" beam with ions positioned at intensity nulls has been predicted to offer significant improvements simultaneously in cooling rate, bandwidth, and final phonon number [31,32], but has not previously been experimentally realized. Importantly, due to the SW EIT scheme's complete suppression of both first-order carrier and blue sideband transitions in favor of the red sideband transitions that extract energy from motion, it in principle allows motional mode occupancies below the photon recoil limit and comparable to or below those achievable with resolved sideband cooling, furthermore for multiple modes simultaneously and at significantly higher rates.

In this work, we experimentally demonstrate fast, broadband laser cooling in nodal positions of integrated SW drive fields. We measure Doppler cooling to below the Doppler limit for a trapped ion positioned at SW nodes, realizing a long-standing prediction and verifying the basic mechanism. We further experimentally demonstrate SW EIT ground-state cooling of radial motional modes to phonon occupancies $\bar{n} \approx 0.05$, and all single-ion motional modes spanning a 5 MHz bandwidth close to the ground state ($\bar{n} \lesssim 1$), within 150 μs starting from near the Doppler limit. The foundry-fabricated trap devices utilized in this work incorporate running-wave (RW) beam delivery that allows direct experimental comparison between the carrier-nulled SW scheme and the RW equivalent. We thereby demonstrate SW EIT's simultaneous advantages in motional mode bandwidth, cooling rate, and final phonon number. We present detailed simulations of limiting non-idealities in our apparatus that indicate straightforward design optimizations would reduce the final phonon number limit by over an order of magnitude further, to the limits imposed by current technical noise levels. This work realizes fast, multi-mode ground-state cooling, addresses a significant operation time limitation in trapped-ion QC systems, and demonstrates a clear performance advantage practically enabled by scalable optical control of atomic systems.

In the following, we first review the basic mechanisms and intuition behind the cooling schemes demonstrated here. We then describe the experimental platform and apparatus utilized and present characterization of the photonics spanning ultraviolet (UV) to near infrared (NIR) wavelengths employed in the trap device, including profiling of the UV SW using a single $^{40}Ca^{+}$ ion as a high-resolution probe. We thereby characterize the extinction realized at the SW nodes, along with our ability to precisely position the atom in this spatially varying intensity profile. We present results demonstrating Doppler cooling to below the Doppler limit at SW nodes for multiple modes, followed by SW EIT cooling of all single-ion modes to near the ground state. We perform direct evaluation against the comparable RW EIT scheme to verify the SW field's role and the relative performance of the two schemes. Experimental details and numerical simulations quantifying technical limitations on the observed performance are presented in the Appendix, indicating concrete routes to further improvement. We conclude with a discussion of these straightforward improvements and the expected resulting performance, the fundamental limits of the cooling scheme demonstrated here, and extensions to multi-ion crystals.

II. CARRIER-NULLED COOLING MECHANISM

The enhancements to both Doppler cooling and EIT ground-state cooling demonstrated here rely on a similar basic mechanism [29,31,32] which we briefly review in this section. Figure 1(a) shows the level structure for a closed two-level system of frequency ω_0, driven by a cooling laser field with amplitude Ω_c. Considering one mode of motion at frequency ω_m of such an atom in a harmonic trap, in addition to the "carrier" transition, resonant at drive frequency ω_0, resonant transitions at $\omega_0 \pm \omega_m$ add or substract a quantum of motion upon internal state excitation, referred to as "blue" and "red" sideband transitions (RSB and BSB, respectively) and indicated by the blue and red lines in Fig. 1(a). For atoms with wavefunction extent small compared to the wavelength (the Lamb-Dicke regime) [33] where first-order sidebands dominate, the carrier transition and these sideband transitions approximate the full behavior. For a two-level system with electric dipole moment, the carrier transition has amplitude Ω_c proportional to the electric field strength at the ion location. The sideband transitions have amplitude proportional to the field gradient, $\eta\Omega_c$, with η the Lamb-Dicke parameter, well below unity for typical parameters. Hence for light delivered as a phase-stable standing wave [Fig. 1(b)] to an atom positioned at a node where only the field gradient is nonzero, the carrier is nulled and only sidebands are driven.

Cooling is generally achieved via excitation in a manner that preferentially drives RSB transitions. Figure 1(c) shows the excited-state population and hence spontaneous scattering rate as a function of a cooling beam detuning for an atom at rest. A RW cooling beam at $\Delta_c = -\Gamma/2$ results in optimal contrast between RSB and BSB scattering rates; however the strong carrier transition is also driven, resulting in additional photon scattering that heats the ion motion. When Ω_c is instead delivered as a SW and the ion positioned at a node, this carrier scattering is nulled, resulting in an approximately 2× lower cooling limit [29], quantified by the steady-state expectation phonon number $\bar{n}_{ss}$. Additionally, carrier suppression reduces power broadening of the line at high Ω_c which in turn would reduce

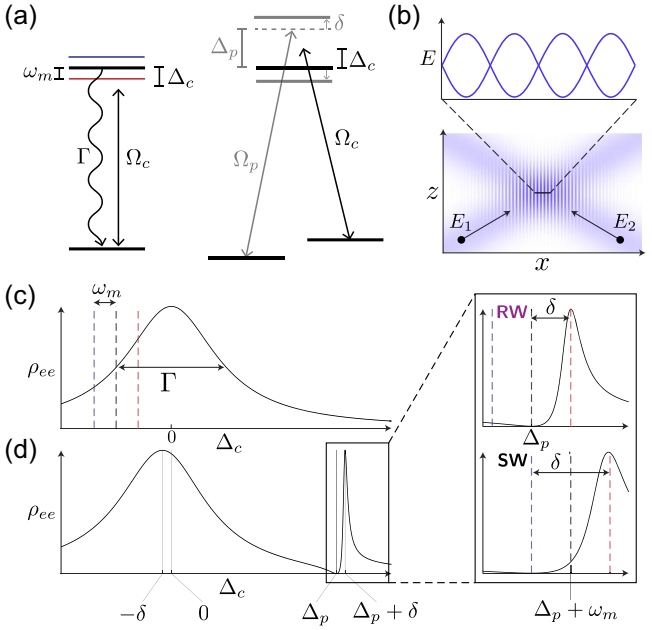


FIG. 1. General mechanism behind SW cooling schemes demonstrated. (a) Basic level structures relevant to Doppler (left) and EIT cooling (right), with symbols as defined in the main text. Blue and red lines (shown only on the left for simplicity) indicate motional sideband transitions that raise or lower n of a mode of frequency ω_m. (b) Phase-stable beams counterpropagating along x and polarized along y in this illustration result in a standing-wave intensity profile; atoms confined at nodes experience maximum gradient that drives sideband transitions only, with nulled carrier excitation. (c) Excitation spectrum of the Ω_c beam for Doppler cooling. When Δ_c is chosen at $-\Gamma/2$; probabilities of RSB and BSB scattering are proportional to ρ_{ee} at the red and blue dashed lines, and similarly for carrier scattering in a RW at the black dashed line. (d) Ω_c excitation spectrum for EIT cooling in the presence of Ω_p at fixed Δ_p. Insets show choice of pump beam strength Ω_p and resultant ac stark shift δ_{EIT} for optimal cooling of a mode of motional frequency ω_m, for the Ω_c beam delivered as a RW, or as a SW.

contrast in the RSB and BSB scattering rates; this reduced saturation allows SW cooling to operate at higher Ω_c and hence cooling rates both within and beyond the LD regime [29,32].

A similar concept can be applied to EIT cooling, with more significant improvement in the cooling performance. EIT cooling utilizes a three-level electronic system driven by a strong pump beam (Ω_p, Δ_p) [Fig. 1(a)] which modifies the atomic response to a temporally coherent "cooling" or "probe" beam (Ω_c, Δ_c). Excitation is suppressed at the two-photon resonance $\Delta_c = \Delta_p$, with bright resonances ac Stark shifted by $\delta_{\mathrm{EIT}} = \frac{1}{2}(\sqrt{\Omega_p^2 + \Delta_p^2} - \Delta_p)$ from either the single- ($\Delta_c = 0$) or two-photon cooling beam resonance conditions (gray lines) [34]. As shown in Fig. 1(d), RW EIT uses the dark resonance to suppress carrier excitation by setting $\Delta_c = \Delta_p$; by choosing Ω_p and Δ_p to set $\delta_{\mathrm{EIT}} = \omega_m$, the narrow bright resonance results in strong contrast between the RSB and BSB scattering rates, and much lower $\bar{n}_{\mathrm{ss}}$ limits as compared to Doppler cooling [14,15]. However the finite BSB excitation rate still limits $\bar{n}_{\mathrm{ss}}$ values achievable, and the strong carrier coupling on the Ω_c beam again limits cooling rates. Delivery of Ω_c as a SW and setting $\delta_{\mathrm{EIT}} = 2\omega_m$ allows for a different choice of Δ_c [Fig. 1(d)] that leverages the *spatial* coherence of the interfering fields to null carrier excitation, and uses the EIT dark resonance to perfectly null BSB excitation. This results simultaneously in dramatically lower $\bar{n}_{\mathrm{ss}}$ values achievable, comparable to or even below resolved sideband cooling; significantly broader cooling bandwidth, i.e. the range of motional mode frequencies around the target ω_m that can be effectively cooled; along with higher cooling rates [32].

III. EXPERIMENTAL SYSTEM

The relevant energy levels and transitions of the $^{40}Ca^{+}$ ions used in this work are shown in Fig. 2(a). We use a foundry-fabricated ion trap chip device with both silicon nitride (Si_3N_4) [35] and aluminum oxide (Al_2O_3) waveguides [36–38] to deliver all required wavelengths for $^{40}Ca^{+}$ ion control. The device layer stack-up is shown in Fig. 2(b). Devices are fabricated on 100-mm-diameter Si substrates, with thin-film Si_3N_4 and Al_2O_3 patterned via electron-beam lithography to define photonic elements for coupling, splitting, routing, and beam-forming. In this work, Al_2O_3 is used for the blue and UV wavelengths ($\lambda = 375$, 397, and 422 nm) and Si_3N_4 for visible and near-IR wavelengths ($\lambda = 729$, 854, and 866 nm). The latter are of the same cross section as employed in previous work [18]. The top Ti/Au layer forms a surface-electrode Paul trap [39] designed to confine ions 50 μm above the top surface. The openings for beam delivery from waveguides to the ion are coated with a 20-nm-thick conductive indium-tin-oxide (ITO) layer [17], intended to shield the ion from stray charge on exposed dielectrics, including light-induced charging. Underneath the trap electrodes, a gold ground plane is formed to shield the silicon substrate from rf fields and the ions from the mobile charge carriers in the substrate [40,41].

Figure 2(c) shows a schematic of the trap zone and beam configuration used in this work, with waveguide channels and couplers for wavelengths used for photoionization ($\lambda = 375$ and 422 nm), optical transition coherent control (729 nm), repumping (854 and 866 nm), and state preparation, laser cooling, and readout (397 nm). Two grating couplers ("SW1" and "SW2") fed by the same 1×2 multi-mode interferometer (MMI) splitter emit at $\theta = 60°$ from the trap normal to intersect 50 μm above the trap surface, forming a phase-stable $\lambda = 397$ nm SW in the $x - y$ plane. These are oriented along a line at $-45°$ to

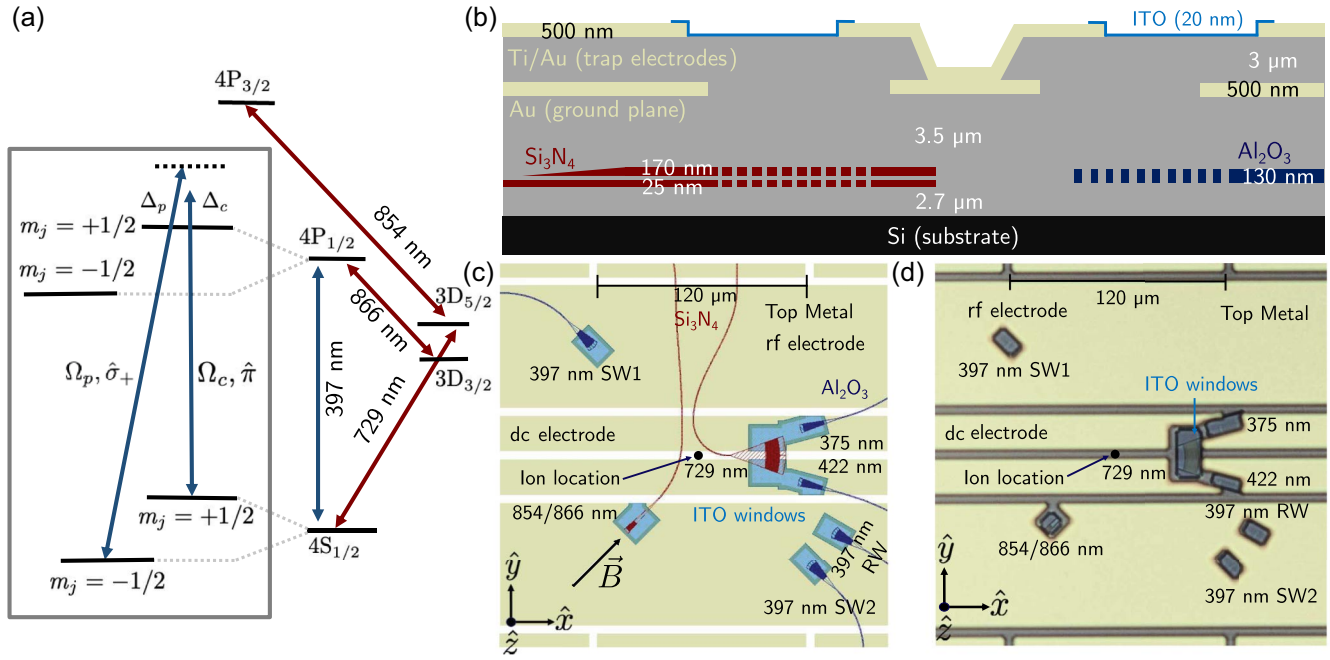


FIG. 2. Experimental platform and ion trap device delivering the required wavelengths. (a) Relevant energy level structure of $^{40}Ca^+$. $\lambda = 397$ nm transitions are used for laser cooling and state readout; light at 729 nm drives an electric quadrupole transition for spectroscopy and motional diagnostics; and 854 and 866 nm serve as repumpers. Δ_p and Δ_c denote the detuning of the EIT pump ($\hat{\boldsymbol{\sigma}}_+$) and the probe beam ($\hat{\boldsymbol{\pi}}$) from the $|4S_{1/2}, m_j = -1/2\rangle \leftrightarrow |4P_{1/2}, m_j = +1/2\rangle$ and the $|4S_{1/2}, m_j = +1/2\rangle \leftrightarrow |4P_{1/2}, m_j = +1/2\rangle$ transitions respectively. (b) Layer stack-up schematic, incorporating waveguide features for routing and emission in a 130-nm-thick Al_2O_3 layer and in Si_3N_4 layers of 25 and 170 nm thickness. A 500-nm-thick Au layer (using Ti for adhesion) forms both the ground plane and the top rf and dc electrodes. A 20-nm-thick conductive ITO film is used to mitigate potential surface charging at top electrode openings. (c) Layout of the trap zone used, and the integrated waveguide and grating elements at the indicated wavelengths, B-field orientation, top metal, and ITO features. Additionally, free-space $\lambda = 397$ nm beams are employed for the $\hat{\boldsymbol{\sigma}}_+$ EIT pump and for the $\hat{\boldsymbol{\pi}}$-polarized RW Doppler cooling beam, propagating parallel to the trap surface along and perpendicular to $\vec{B}$, respectively. (d) Bright-field microscope image of the same zone.

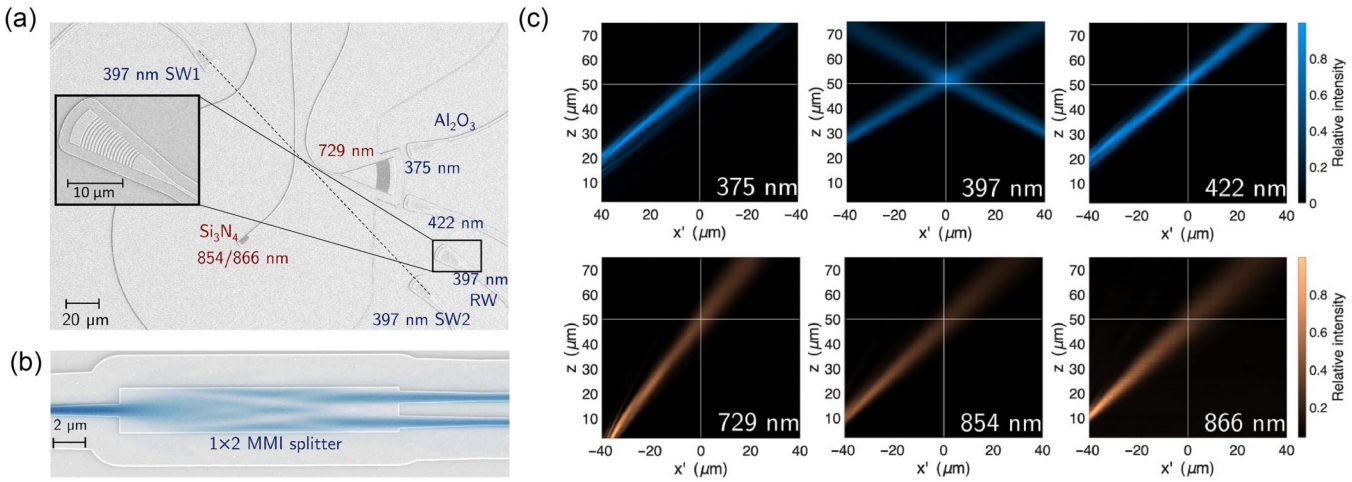


FIG. 3. Integrated optical component characterization. Scanning electron microscope (SEM) images of (a) fabricated Al_2O_3 and Si_3N_4 waveguides features near the trap zone employed in this work, following waveguide fabrication and prior to cladding and metallization. (b) The $1 \times 2 Al_2O_3$ MMI splitter, overlaid with the simulated intensity profile for $\lambda = 397$ nm, feeding the "SW1" and "SW2" grating couplers. (c) Measured grating emission profiles at the labeled wavelengths along the "longitudinal" direction x' for each grating [e.g., dashed line in (a) for the SW couplers], obtained from images of the radiated fields of the integrated grating couplers at different heights above the trap electrode; line crossings indicate the target ion position, demonstrating realized targeting accuracy of $\lesssim 2$ μm for all wavelengths.

the trap axis $\hat{\boldsymbol{x}}$ to produce wave vector components along the axial and both radial motional modes, and a $\hat{\boldsymbol{\pi}}$-polarized field when fed with quasi-TE waveguide modes given the orientation of the quantizing magnetic field. A separate coupler oriented −34° to the trap axis delivers the RW EIT probe beam, also approximately $\hat{\boldsymbol{\pi}}$-polarized. For EIT cooling, these $\hat{\boldsymbol{\pi}}$-polarized fields couple $|4S_{1/2}, m_j = +1/2\rangle$ and $|4P_{1/2}, m_j = +1/2\rangle$, while the $\hat{\boldsymbol{\sigma}}_+$-polarized beam serving as the EIT "pump" coupling $|4S_{1/2}, m_j = -1/2\rangle$ and $|4P_{1/2}, m_j = +1/2\rangle$ is delivered via free-space optics and propagates along the magnetic field direction. An optical microscope image of the fabricated trap zone is shown in Fig. 2(d), with scanning electron microscope images of the waveguide features shown in Figs. 3(a) and 3(b), respectively.

Figure. 3(c) shows measured longitudinal emission profiles of the gratings at the designed wavelengths, profiled using a scanning imaging system with a scientific CCD camera [42]. We measure a targeting inaccuracy of less than 2 μm for all wavelengths, indicating the functioning of the optical components in accordance with design and simulation. This allows the experiments presented below to efficiently utilize delivery of the other required wavelengths via fiber-coupled waveguide paths alongside the $\lambda = 397$ nm light most directly implicated in the cooling schemes studied.

For cryogenic ion trap experiments, light is delivered to the integrated waveguides via a 14-channel fiber V-groove array (VGA) populated with single-mode fibers for both UV and visible/NIR wavelengths. The VGA and trap chip are aligned to each other and mutually attached to a common carrier PCB in a fashion compatible with both cooling and thermal cycling to the 4.8 K experimental operation temperature, as well as UV delivery without photodamage. In this work, all $\lambda = 729$, 854, and 866 nm light is delivered through the integrated channels. The integrated SW and RW $\lambda = 397$ nm paths are used for SW and RW cooling beam delivery for EIT experiments. Photoionization to load the trap utilizes the integrated $\lambda = 422$ nm path and a free-space $\lambda = 375$ nm beam. A free-space $\hat{\boldsymbol{\sigma}}_+$-polarized $\lambda = 397$ nm beam is used for state preparation and as the EIT pump beam, and a free-space $\hat{\boldsymbol{\pi}}$-polarized beam for RW Doppler cooling and readout. Further details on the full device layout and packaging are provided in the Appendix.

IV. SW PROFILING AND CHARACTERIZATION

We use a single $^{40}Ca^+$ ion as a high-resolution field probe, and as a means to evaluate positioning stability in the UV SW generated via the on-chip optics. We control the ion position via dc voltages applied to the trap electrodes and characterize the SW profile by measuring the ac Stark shift δ on a narrow-linewidth optical quadrupole transition as a function of ion position along the trap axis (controlled via dc voltages applied to the trap electrodes), with $\lambda = 397$ nm light detuned by Δ_{397} from the $|4S_{1/2}\rangle \leftrightarrow |4P_{1/2}\rangle$ transition incident through the SW couplers. We use a small detuning $\Delta_{397}/2\pi = -1$ GHz such that δ is dominated by the ac stark shift of $|4S_{1/2}, m_j = +1/2\rangle$.

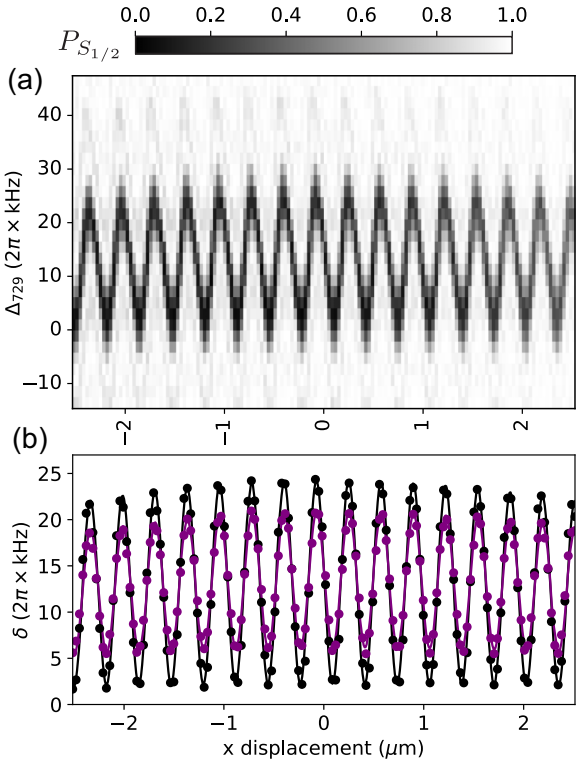


FIG. 4. SW profiling via ac Stark shift measurements on the optical quadrupole transition. (a) Population $P_{S_{1/2}}$ remaining in $|4S_{1/2}\rangle$ after a π pulse on the $|4S_{1/2}, m_j = +1/2\rangle \leftrightarrow |3D_{5/2}, m_j = +1/2\rangle$ carrier transition, with $\lambda = 397$ nm light detuned by $\Delta_{397}/2\pi = -1$ GHz sent to the SW couplers. The measurement is taken for varying axial displacements of the ion, with axial mode initially cooled to the ground state via RW EIT cooling for this data. $\Delta_{729} = 0$ corresponds to the quadrupole transition frequency calibrated with no light in the SW. (b) Corresponding fit ac stark shift on $|4S_{1/2}, m_j = +1/2\rangle\delta$ vs axial displacement (black), along with that measured only after Doppler cooling (purple). Lines correspond to a fit SW profile with Gaussian amplitude envelope. The contrast near the SW center at 0 displacement for ground-state-cooled ions yields a Stark shift extinction ratio $\gamma \equiv \delta_{\text{an}}/\delta_{\text{n}} = 10.83(3)$. 1σ error bars are smaller than data points.

After laser cooling and optically pumping the ion into the $|4S_{1/2}, m_j = +1/2\rangle$ state, we measure δ via spectroscopy on the $|4S_{1/2}, m_j = +1/2\rangle \leftrightarrow |3D_{5/2}, m_j = +1/2\rangle$ with a $\lambda = 729$ nm probe pulse detuned Δ_{729} with respect to the unshifted resonance, applied simultaneously with the SW light. Figure 4(a) shows the resulting populations $P_{S_{1/2}}$ remaining in the electronic ground state, measured as a function of Δ_{729} and the ion position along the axial

direction $\hat{\boldsymbol{x}}$, for an ion with axial motion initially cooled to the quantum ground state. Fits of the excitation spectrum at each position allow determination of δ, which are shown (with fits to a Gaussian-envelope SW profile) in Fig. 4(b). Fit δ values for the data in panel (a) are shown in black, and additionally for ions initially cooled only to the Doppler limit in purple.

We define the ac Stark shift extinction ratio in the SW, $\gamma \equiv \delta_{\mathrm{an}}/\delta_{\mathrm{n}}$, as the ratio of the ac Stark shift at the antinode, δ_{an} and at the node, δ_{n}. Due to optical coupling to sideband transitions, or equivalently as due to the spatial dependence of the ac Stark shift on the ground state [43], even for an optical profile with perfect intensity extinction at the SW nodes, δ_{n} scales with the wavefunction extent and phonon number of motional modes with mode vector projection along the SW direction (see Appendix F). As a result, we measure a larger γ after ground-state cooling of the axial mode (black points and fits) as compared to simply after Doppler cooling (purple). Near the center of SW profile, the fits indicate $\gamma = 10.83(3)$ for ground-state-cooled ions. Measured phonon numbers and associated wavefunction extent after the cooling employed would result in $\gamma_0 \approx 20$ (see Appendix F). The difference between γ_0 and our measured γ would be explained by residual carrier coupling at the node with Rabi frequency 9.5% of the SW antinode. Approximately 20 nm-level fluctuations in trap position on timescales shorter than those over which we average for the Stark shift measurements would account for the discrepancy between γ_0 and γ, which may be due to E-field noise and resulting jitter in the equilibrium trap position (see Appendix F).

V. SW DOPPLER COOLING

We employ the demonstrated SW extinction, as well as stable ion positioning in the UV SW, to explore SW Doppler cooling to phonon numbers below the typical Doppler limit. In our experiment, the free-space RW and the integrated SW beams used for Doppler cooling have the same wave vector direction in the $\hat{\boldsymbol{x}} - \hat{\boldsymbol{y}}$ plane, allowing simultaneous cooling of all three motional modes (see Appendix E). We iteratively scan the RW and SW cooling beams' detuning, intensity, and pulse duration to first minimize the decoherence of Rabi oscillations on a $\lambda = 729$ nm transition due to the ion's motion and then the phonon numbers of the R_2 mode via a more precise method based on imbalance in motional sideband excitation of a $\lambda = 729$ nm optical quadrupole transition [44]. Both the optimized RW and SW detunings are consistent with $\Delta = -\Gamma/2$ given the $P_{1/2}$ natural linewidth $\Gamma \approx 2\pi \times 21.5$ MHz. Finally, with the optimized cooling beam parameters, we measure the resulting phonon number via the sideband imbalance method for all three motional modes.

Prior to cooling within experimental sequences, ions are expected to have axial mode occupancies $\bar{n}_{\mathrm{ax}}$ of order 100 due to scattering during the preceeding readout (see Appendix D). As reported in Table I, after 1500 μs of RW Doppler cooling the phonon numbers in all three modes approach the standard RW Doppler limit $\simeq \frac{\Gamma}{2\omega_m}\left(\frac{1}{2} + \frac{\alpha}{\cos^2\theta_m}\right)$, for motional frequency ω_m, angle between the cooling beam and motional direction θ_m, and coupling of isotropic spontaneous emission into any motional axis $\alpha = 1/3$ [45,46].

TABLE I. Theoretical and experimental (with 1σ uncertainty) final phonon numbers. From left to right, columns correspond to theoretical limit of RW Doppler cooling; and measured $\bar{n}_{\mathrm{ss}}$ values after 1500 μs Doppler cooling with the RW, 700 μs with the SW and ion positioned at a node, or both, on all three motional modes.

	RW limit	RW	SW	RW & SW
Axial (1.18 MHz) $\bar{n}_{\mathrm{ss}}$	10.6	12(2)	6.9(6)	6.4(5)
R_1 (4.45 MHz) $\bar{n}_{\mathrm{ss}}$	4.4	4.2(5)	2.5(2)	2.4(2)
R_2 (5.27 MHz) $\bar{n}_{\mathrm{ss}}$	3.7	2.7(4)	1.7(1)	1.7(1)

For SW Doppler cooling, we can apply varying strengths of the carrier and sideband interactions by translating the ion through the SW profile. Figure 5 shows the measured $\bar{n}$ in the R_1 radial mode following SW after RW Doppler cooling, as a function of trap displacement along the axial direction. In contrast to the SW nodes at which the ion is cooled to below the Doppler limit, at the SW antinodes, the field gradient is zero, which leads to no sideband excitation and only heating from carrier excitation [29]. The regular dependence of $\bar{n}$ with axial position and the correspondence to the SW periodicity confirm the SW's role in cooling, and the ability to leverage phase-stable delivery for motional control.

For an ion positioned at a SW node, SW Doppler cooling of 700 μs duration with or without preceding RW cooling brings the phonon number in the axial mode to

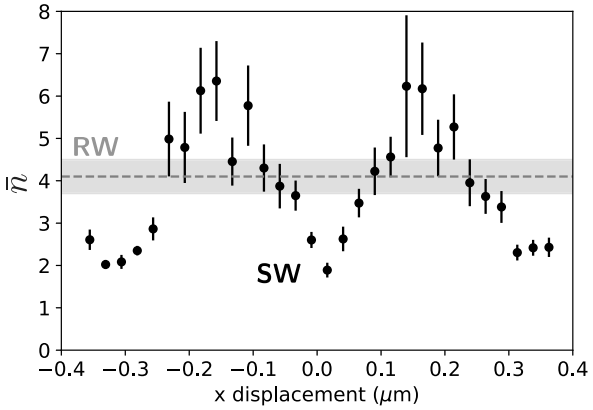


FIG. 5. Final R_1 mode phonon number after SW Doppler cooling (black points) as a function of axial position. Dashed line and uncertainty indicates the $\bar{n}$ measured after RW cooling. Zero displacement corresponds to the central SW node. Error bars indicate 1σ uncertainty.

$\sim$1.8$\times$ below the RW Doppler limit, with similar enhancement factors in cooling limit observed for the radial modes (Table I). These cooling limits are lower by close to the factor of two predicted within the Lamb-Dicke (LD) regime [29]. The agreement between values of final phonon number $\bar{n}_{ss}$ measured with and without RW Doppler cooling also indicates the effectiveness of SW Doppler cooling even from well beyond the LD regime [32].

VI. GROUND-STATE SW EIT COOLING

Having demonstrated simple cooling dynamics in the phase-stable SW, we turn to ground-state EIT cooling for which enhancements of greater practical significance are predicted in SW configurations [32].

In our experiment, the three-level system consists of the two $4S_{1/2}$ ground states, and $|4P_{1/2}, m_j = +1/2\rangle$. We employ a free-space $\hat{\boldsymbol{\sigma}}_+$-polarized pump beam with $\Delta_p \approx 2\pi \times 120$ MHz, and approximately $\hat{\boldsymbol{\pi}}$-polarized cooling beams originating either from the integrated SW couplers, or the RW coupler (Fig. 2) for a direct comparison between RW and SW cooling. Note that the cooling axis in RW EIT is the wave vector difference between the pump and cooling beam; for SW EIT it is simply the SW wave vector itself. Both RW and SW cooling axes have considerable projection along radial and axial modes (see details on mode orientations in Appendix E). Here, we tune Ω_p to optimally cool the R_1 mode for both RW and SW EIT cooling and measure the resulting phonon number in all modes to directly compare the performance of RW and SW EIT in terms of cooling rate, limit, and bandwidth.

We use two sets of Ω_p and Δ_c according to theoretical expectations for RW and SW EIT cooling targeting the R_1 mode. We set the ac Stark shift from Ω_p on $|4S_{1/2}, m_j = -1/2\rangle$ to the expected value using the inverse ac Stark shift sequence described in Appendix D. With Ω_c below saturation, we also vary Ω_p and Δ_c to confirm that the chosen values minimize $\bar{n}_{ss}$ for both RW and SW EIT. Lastly, we minimize the cooling duration by increasing Ω_c.

Figure 6 shows the measured phonon numbers for all motional modes as a function of cooling duration, for optimal RW and SW EIT cooling parameters chosen to cool the first radial mode R_1 with frequency $\omega_{R_1} = 2\pi \times 4.45$ MHz, and with the ion positioned at the node of the SW cooling beam in the latter case. We fit the cooling trajectories to $\dot{\bar{n}}(t) = -W_c \bar{n}(t) + R_h$, with W_c the cooling rate and R_h the total heating rate and from which we infer $\bar{n}_{ss} = R_h/W_c$; results of the fits and final $\bar{n}$ values achieved are summarized in Table II. RW EIT of 500 μs duration on the target R_1 mode has W_c and $\bar{n}_{ss}$ comparable to previously demonstrated results [14,15], but negligibly affects the other two motional modes. On the other hand, $\sim$150 μs of SW EIT cooling brings this mode to $\bar{n}_{ss} = 0.050(3)$ within a shorter duration. At the same time,

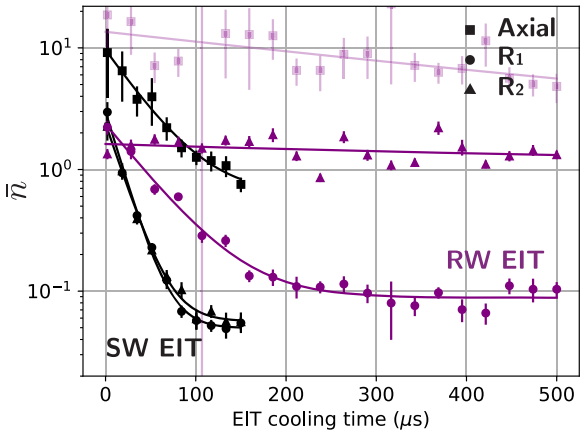


FIG. 6. RW and SW EIT cooling dynamics. The expectation phonon number in all three motional modes is measured as a function of cooling time for both RW and SW EIT, in all cases with cooling parameters optimized for the R_1 mode. Corresponding final phonon numbers and cooling rates are listed in Table II (see raw data of the sideband imbalance measurement used to infer $\bar{n}$ after EIT cooling in the appendix). Error bars indicate 1σ uncertainty.

SW EIT significantly reduces the phonon numbers in the other two motional modes. In particular, despite both optimized on a mode of $\sim$4$\times$ higher frequency, RW EIT weakly cools the axial mode while SW EIT brings it to $\sim$10$\times$ below its Doppler limit, clearly demonstrating the SW scheme's higher cooling bandwidth [32]. Due to increased positional drifts observed at high emitted intensities (see Appendix I), we operate at Ω_c well below that at which the SW EIT cooling rate would saturate, indicating potential for further future improvements in W_c.

Our experimentally observed $\bar{n}_{ss}$ values are significantly above the $< 10^{-4}$ levels theoretically possible with SW EIT cooling [32]. As detailed in Appendix H, key experimental limitations to $\bar{n}_{ss}$ in our experiments arise from, in order of importance: (1) $\hat{\boldsymbol{\sigma}}_+$ beam polarization impurity arising from quantization axis oscillations due to

TABLE II. Final phonon numbers and cooling rate (with 1σ uncertainty) of cooled motional modes after 500 μs RW EIT or 150 μs SW EIT cooling optimized for the R_1 mode. For well-cooled modes, we fit cooling trajectories to extract W_c and $\bar{n}_{ss}$; for weakly cooled modes, fit results were relatively unreliable, and we report the final measured $\bar{n}$, marked with asterisks. RW EIT cooling rates of the negligibly cooled axial and R_2 modes are omitted due to high uncertainty.

	RW EIT		SW EIT	
	$\bar{n}_{ss}$	W_c (ms^{-1})	$\bar{n}_{ss}$	W_c (ms^{-1})
Axial	5(1)*		0.8(1)*	25(3)
R_1	0.088(5)	21(2)	0.050(3)	57(3)
R_2	1.3(1)*		0.056(4)	52(3)

trap rf-induced magnetic fields [47,48], resulting in ∼0.6% relative intensity in the $\hat{\boldsymbol{\pi}}$ component in our current system (2) positional fluctuations and/or imperfect SW optical extinction that result in residual intensity at the SW node; and (3) motional heating rates. As quantified in our master equation simulations (Appendix H), these known nonidealities limit the achievable $\bar{n}_{\mathrm{ss}}$ to the 10^{-2} level achieved experimentally. While our model explains the order of magnitude of our $\bar{n}_{ss}$ results for both RW and SW experiments, our experimentally measured final phonon numbers are still approximately 2× higher than those predicted from our simulations in the presence of the known nonidealities, likely due to excess technical noise during EIT experimental sequences not accounted for in our independent estimations (see Appendix H). While future experiments will be required to validate our master equation model at significantly lower phonon numbers, our simulations indicate that polarization impurity in the $\hat{\boldsymbol{\sigma}}_+$ beam is the dominant nonideality, and hence that implementation of rf electrode structures that eliminate oscillations in B-field orientation due to trap rf currents would enable SW EIT to reach $\bar{n} \approx 5 \times 10^{-3}$ for the radial modes, an order of magnitude below those observed currently. Reduced electric field noise, and therefore heating and positional fluctuations, could allow yet further reductions toward the $\bar{n} \sim 10^{-5}$ level that is the theoretical limit of the scheme for our parameters, limited by sideband excitations associated with the RW pump beam employed.

Nevertheless, in the presence of all present experimental nonidealities, our experiments demonstrate simultaneous enhancements in cooling limit, rate, and mode frequency bandwidth due to carrier nulling. The realized performance further compares favorably across metrics with polarization gradient cooling recently realized in integrated platforms [27], indicating the promise of SW EIT schemes for fast, broadband laser cooling in integrated settings.

VII. DISCUSSION AND OUTLOOK

Our work suggests various possible improvements to the operations implemented, along with broader possibilities for atomic control in scalable platforms. With respect to SW EIT cooling specifically, integrated delivery of all required beams, including the $\hat{\boldsymbol{\sigma}}_+$ pump, could be implemented by switching to a B-field oriented along the trap surface normal, and a pump beam emitted along the same direction with passive structures emitting pure circular polarization [49–52]. Trap rf electrode routing that minimizes time-varying B-fields perpendicular to the quantization axis would allow SW cooling to reach significantly lower phonon numbers. Operation at higher quantizing magnetic field strengths would further lessen sensitivity to polarization impurities. Straightforward improvements to the fabrication process will further reduce the overall input-to-ion loss, as would higher-efficiency UV gratings based e.g. on higher index-contrast waveguide platforms [53] and/or multi-layer gratings [54]. Together with improved transparent conductive shielding, the resulting higher cooling beam intensities would allow yet higher cooling rates than those demonstrated here and thereby lower $\bar{n}_{\mathrm{ss}}$ values for a given heating rate, as detailed in Appendices H and I.

Two-ion crystals cooled to phonon numbers demonstrated in this work would support laser-based entangling gates with errors due to motional occupancy at the $< 10^{-4}$ level [11]. Achieving such occupancies in a single GS cooling step may alleviate overheads associated with cooling. Fast GS cooling also affects architectural considerations in trapped-ion QC systems, for example in evaluating tradeoffs between laser-based and microwave gates, the latter which can operate at high fidelities with relaxed cooling requirements [55]. We note that even in the case of microwave gates, efficient GS cooling methods may be essential for further fidelity improvements, robustness against compounding imperfections in large-scale systems, and allowing for ion transport at higher speeds and resulting excitations [5]. The sub-recoil limit phonon numbers at the $< 10^{-4}$ levels fundamentally enabled by the SW EIT scheme demonstrated here can eliminate the need for sideband cooling even for the most stringent motional mode occupancy requirements.

The methods demonstrated here can be extended both to multi-ion crystals and more complex internal state structures. Ion chains containing two coolant ions [3,4] may be cooled in SWs oriented as in this work, with positioning requirements comparable to those of many laser-based geometric phase gates [33]. Radial modes of long ion strings with irregular spacings could be straightforwardly addressed either with a SW or Hermite-Gaussian field with nodal line along the axis. EIT cooling has been demonstrated in ions with nonzero nuclear spin and significantly more complex internal structure [56,57], for which we expect similar advantages from carrier nulling. Evaluation of carrier-nulled EIT cooling's performance for highly excited ions would also be an interesting avenue for future work [58].

Concepts similar to those demonstrated here may be applied to systems based on individual neutral atoms requiring ground-state cooling [59–61], including with more general structured light fields [62,63]. The optical addressing and ion positioning precision demonstrated in this work also indicate the practicality of related concepts for quantum logic [26,64–66] in integrated devices, and metrology [67], suggesting broader potential for scalable optical addressing to enhance atomic control at a basic physical level.

ACKNOWLEDGMENTS

We thank Floris Falke, Arne Leinse, and the team at LioniX International for fabrication of the trap devices utilized here, and Sonia Garcia Blanco's group at University of Twente for alumina deposition. We thank Orion Smedley, Alex Shi, and Nelson Ooi for contributions to the apparatus,

Oscar Jaramillo for assistance with SEM imaging, and Jonathan Home for support in the early design stages of this work. We thank John Chiaverini and Jonathan Home for comments on the manuscript. We acknowledge support from an NSF CAREER Grant (No. 2338897); IARPA and the Army Research Office, under the Entangled Logical Qubits program, Cooperative Agreement No. W911NF-23-2-0216; the NSF NQVL program (No. 2435382); the Alfred P. Sloan Foundation; and Cornell University. The views and conclusions contained in this document are those of the authors and should not be interpreted as representing the official policies, either expressed or implied, of IARPA, the Army Research Office, or the U.S. Government. The U.S. Government is authorized to reproduce and distribute reprints for Government purposes notwithstanding any copyright notation herein.

DATA AVAILABILITY

The data that support the findings of this article are openly available [68].

APPENDIX A: DEVICE DESIGN AND FABRICATION

Trap devices were fabricated at LioniX International, with support from the University of Twente for Al_2O_3 deposition, on 100-mm-diameter wafers. The layer stack used is similar to previous work [23] using this foundry platform, but additionally incorporating Al_2O_3 waveguides for low-loss light delivery at blue and UV wavelengths, indium tin oxide (ITO) as a transparent conductor to shield windows in the top metal introduced to allow light propagation out of the device [17], and utilizing gold for both top metal and ground plane layer. All waveguide features were fabricated using electron beam lithography in this work.

Emitting gratings were designed according to the methods presented in Ref. [69], and simulated with full 3D FDTD (Ansys Lumerical FDTD and Tidy3D). The 1×2397 nm MMI splitter used for the SW generation has a simulated excess loss of 0.21 dB. Simulated grating losses for the designs presented in Fig. 3 range from 3 dB for the Si_3N_4 designs for 729 nm wavelength, to 8 dB for present blue/UV wavelengths in Al_2O_3. The latter efficiencies are limited by the relatively low refractive index contrast between Al_2O_3 and SiO_2; incorporation of higher refractive index contrast core materials for blue/UV waveguides [53] and/or multi-layer gratings [54] would enable higher efficiency gratings of the same footprint.

Input couplers to the on-chip waveguides rely on lateral tapers for the Al_2O_3 waveguides, which taper down to 150 nm width at the fiber-coupling edges [the left edge in Fig. 7(a)], to result in weakly confined modes relatively well matched to optical fiber modes. The same vertical taper designs used in Ref. [18] were used for the Si_3N_4 waveguides. After fabrication of the Al_2O_3 waveguides on the present devices but prior to the SiO_2 cladding deposition, delamination of the narrow waveguides within approximately 300 μm of the intended input coupling chip edge was observed, due to poor adhesion of narrow Al_2O_3

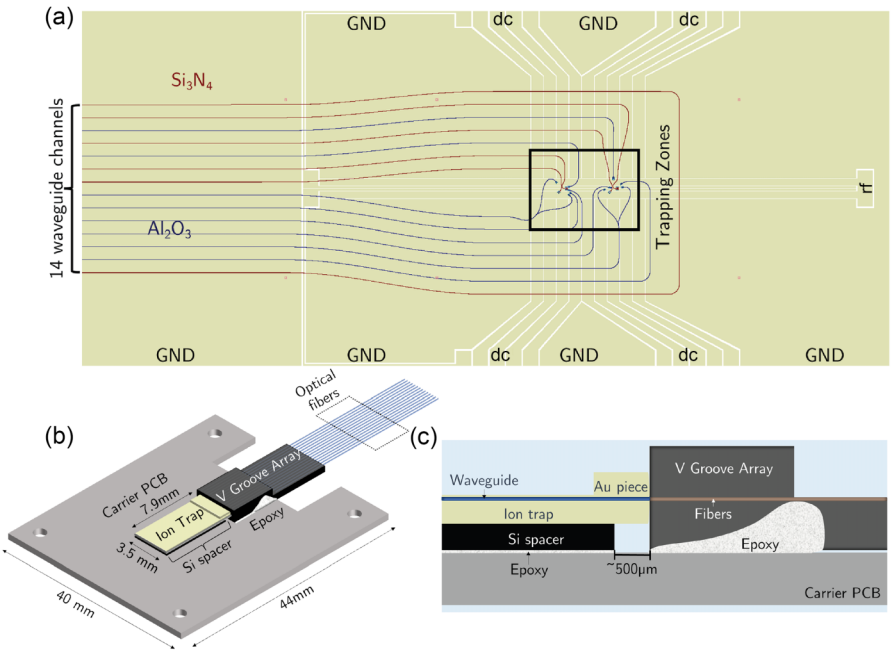


FIG. 7. Ion trap chip design and schematic assembly. (a) Design layout of the ion trap device showing Al_2O_3 and Si_3N_4 waveguide features, and dc and rf electrode configurations. (b) Schematic of fiber V-groove array (VGA) and trap device mounting on the carrier board fixed to the 4 K experimental chamber. (c) Side view of the fiber VGA attachment.

features to the substrate; this issue was present only where the Al_2O_3 waveguide features were narrow. As a result, chip die were diced at that facet approximately 350 μm inwards from where originally intended, at such a distance in from the originally intended facet that the lateral taper had expanded to a width that remained fixed to the thermal SiO_2 beneath the waveguides. While this allowed input coupling to all channels, it resulted in somewhat higher edge-coupling losses on all channels than expected, as discussed below. This issue can be straightforwardly avoided by incorporating large-area Al_2O_3 features off the actual trap die to anchor the narrow laterally tapered waveguides in future fabrication runs.

APPENDIX B: TRAP ASSEMBLY, PACKAGING AND POWER HANDLING

On-chip waveguide channels [see Fig. 7(a)] are fed by a fourteen-channel V-groove array (VGA), supplied by OZ Optics. The VGA is populated with Fibercore SM300 and Nufern S630-HP fibers with 127 μm pitch, to deliver light to Al_2O_3 and Si_3N_4 waveguides, respectively. We use the outer two channels to align the VGA with the trap device by maximizing transmission through the outer Si_3N_4 waveguide loop visible in Fig. 7(a).

We polish with a method similar to [18] to reduce roughness from dicing and loss associated with the coupling interface of the ion trap chip. To facilitate polishing, a piece of 1.2×3.3 mm^2 SiO_2 with 500 μm thickness is coated with 500 nm of gold (to prevent possible stray field from the exposed dielectric) and attached with a conductive epoxy (EPO-TEK, model H21D) to the top surface of the trap chip at the fiber-coupling edge shown in Fig. 7. Subsequently, we spin-coat the chip in a protective photoresist (FSC M) and mount it in a custom-made holder for facet polishing. Because our devices contain nearly twice as many optical channels as those in Ref. [18], we employ a polishing holder designed to minimize lateral curvature of the facet and hence the air-gap between fibers and waveguides.

The trap chip's Si substrate thickness (500 μm) differs from that of the VGAs used (1 mm). To match the waveguide and fiber heights, we attach a Si piece of 3.5×7 mm^2 dimension and 500 μm thickness to the carrier PCB using EPO-TEK T7110 epoxy, as a "pedestal" on which to mount the trap [see Fig. 7(b)]. In addition to matching the waveguide height to that of the VGA substrate thickness (1 mm), the epoxy thickness (roughly 50 μm) results in a small gap between the VGA substrate and the PCB, providing clearance to position the VGA for fiber attachment. Subsequently, we scribe the Si substrate of the die to break through the native oxide and remove the protective photoresist. We attach the die to the Si pedestal using EPO-TEK 301-2FL epoxy (epoxy without filler) to minimize the gap between the Si pedestal and the trap chip. Furthermore, we leave an approximately 500 μm distance [see Fig. 7(c)] between the fiber coupling edge of the trap die and the edge of the Si spacer on the fiber coupling side, which is crucial to prevent epoxy from wicking between the VGA and the trap interface during VGA attachment. We apply a drop of conductive silver epoxy (EPO-TEK, model H21D) on both sides of the trap chip near where the native oxide was scribed to contact the Si substrate, gold-coated SiO_2 piece, and the ground of the trap metal to the ground of the carrier PCB. We wirebond the trap electrodes to the carrier PCB (gold electrodes) using 25-μm-diameter gold wire with a wedge wirebonder.

To attach the fiber array, we clamp the carrier PCB in a custom mount heated to 90 °C, 10 °C above the glue curing temperature. The VGA is clamped to a Thorlabs HFA001 fiber array holder and mounted on a 6-Axis NanoMax Stage (Thorlabs MAX603D) for automatic alignment by maximizing the transmission through the loop waveguides shown in Fig. 7(a). We use three degrees of freedom (DOF) for automatic alignment, and the other three DOFs are left for manual alignment. After alignment, we press the VGA against the chip so that static friction between the VGA and trap interfaces allows us to passively maintain coupling for multiple hours.

From the total loop transmission, we measure an insertion loss of approximately 5.5 dB/facet at $\lambda = 729$ nm, in comparison to the ∼1.5 dB level loss measured for the same taper couplers in Ref. [18]. We attribute this excess loss to the 350 μm indicing of the trap devices mentioned above, which resulted in an optical mode more highly confined in the Si_3N_4 at the facet and less matched to that of the fiber; the same effect resulted in somewhat higher insertion losses than designed for the Al_2O_3 channels. We manually apply drops of EPO-TEK T7110 epoxy to both sides of the VGA [see Fig. 7(c)], which wicks into the gap between the VGA and the carrier PCB, with the gap between the VGA and the bottom Si spacer preventing the epoxy from wicking into the interface between the trap die and the VGA. We release the VGA after two hours of curing, while the carrier PCB is kept overnight on the heated mount to minimize the risk of uncured epoxy. We measure additional losses of 0.5 and 0.14 dB per facet (at 729 nm) during cool-down from 90 °C to room temperature and from room temperature to 4.8 K, respectively. We attached and cooled down three devices in the same manner and measured similar insertion loss and cool-down behavior. Additionally, we do not observe increased losses after further thermal cycles between room temperature and 4 K.

Prior to the eventually employed method, we fiber-attached several samples following the procedure described in Ref. [18], where epoxy was applied at the VGA-trap interface. Even though the polished facets (smooth at the single nanometer level) are in mechanical contact, at 375 nm, we observed photo-degradation at the fiber feedthrough for input powers as low as 25 μW.

This effect occurred consistently across all tested devices, regardless of the epoxy type (transparent or opaque) or the polishing method. In contrast, the method described above involving no epoxy in the optical path substantially improved UV tolerance, allowing up to 15 mW of 375 nm light (the maximum available laser power) to be delivered without detectable degradation.

APPENDIX C: WAVEGUIDE/GRATING OPTICAL CHARACTERIZATION AND UV WAVEGUIDE LOSS

We profile beams emitted by the various gratings [Fig. 2(c)] using a microscope mounted on a vertical motorized translation stage (Newport TRB12CC). The stage provides 0.25 μm unidirectional positioning accuracy and allows us to image grating emission at different heights above the trap device. The emission was collected through a 0.95 NA objective (Olympus MPLANAPO50x) and imaged onto a scientific CCD camera (Lumenera Infinity 3 S-1UR) [42]. We optimize the input polarization by monitoring the grating emission angle roughly 50 μm above the device. TE polarization emits at a higher angle relative to the normal, owing to the larger effective index in Al_2O_3 and Si_3N_4 waveguides. We measure a targeting inaccuracy below 2 μm for wavelengths spanning 375–866 nm. In addition, we measure waveguide loss of 1.7(3) dB/cm at $\lambda = 397$ nm for quasi-TE modes of single-mode Al_2O_3 waveguides. Si_3N_4 propagation losses were similar to those in Ref. [18].

We infer the total optical loss in the 397 nm SW channel from fiber feedthrough to the ion location by measurement of the differential ac Stark shift of the $|4S_{1/2}, m_j = +1/2\rangle \leftrightarrow |3D_{5/2}, m_j = +1/2\rangle$ quadrupole transition, similar to the measurements presented in Fig. 4. The $\lambda = 397$ nm light is 10 GHz red-detuned from the $S_{1/2} \leftrightarrow P_{1/2}$ transition, such that the quadrupole transition shift is dominated by the ac Stark shift of the $|4S_{1/2}, m_j = +1/2\rangle$ level. At the SW anti-node, we measure $\delta = 2\pi \times 8.04$ kHz for 161 μW power input at the vacuum fiber feedthrough. We calculate the laser intensity I_{SW} at the anti-node corresponding to this ac stark shift from the $S_{1/2} \leftrightarrow P_{1/2}$ dipole transition strengths, and the power emitted in the SW according to the expression $P_{tot} = \frac{1}{4} I_{SW} \pi w_t w_l$. The transverse and longitudinal beam waists $w_t = 8.95$ μm and $w_l = 5.75$ μm, respectively, are obtained from the beam profile measurements discussed above. Through these observations we infer a total loss of 33.3 dB.

This total loss includes fiber connector losses, fiber-to-chip edge-coupling loss, waveguide loss, MMI loss, grating inefficiency, and fiber-mode concentricity; estimates of these contributions are shown in Table III. We find the measured total loss to be ∼10 dB higher than accounted for by these contributions. Potential delamination in the Al_2O_3 waveguide despite the in-dicing may possibly account for the additional loss (this is not directly visible in the fabricated samples coated with metals).

TABLE III. Approximate loss budget for the $\lambda = 397$ nm channel feeding the SW profile. The simulated and measured loss sources account for 20.3–23.1 of the observed 33.3 dB total fiber-to-ion loss; we attribute the remaining ∼10 dB to potential effects of delamination of the narrow input coupling waveguide near edge-coupling facet which occurred on this particular fabrication run.

Loss source	Loss (dB)
Edge coupling (simulated)	3 dB
Additional in-dicing loss (simulated)	4 dB
Fiber connectors	∼4 dB
Grating efficiency (simulated)	8 dB
Waveguide loss (measured)	0.7 dB
MMI splitter (simulated)	0.21 dB
Beam misalignment (measured)	0.5 dB
Fiber core concentricity (simulated)	0–2.8 dB
Total	20.4–23.2 dB

APPENDIX D: LASER SYSTEMS, CRYOGENIC APPARATUS, AND TRAP OPERATION

Ion trap devices are operated at cryogenic temperature (4.8 K) to reduce electric field noise, enhance ion lifetime, and enable rapid reconfiguration. We employ a closed-cycle Gifford-McMahon cryocooler, which is ceiling-mounted and mechanically decoupled from the experiment chamber hosting the trap device to minimize vibrations. The trap chip is mounted in a copper chamber with thick 25.4-cm walls to shield time-varying magnetic fields. A static magnetic field of 8.9 G is generated by permanent magnet rings installed directly the 4 K chamber, generating a quantizing field with simulated fractional uniformity on the level of 10^{-4}/mm near the device center.

We use solid-state diode lasers and frequency doublers (supplied by Toptica Photonics) to deliver all wavelengths except $\lambda = 729$ nm. These diode lasers are frequency-stabilized via a wavelength meter (HighFinesse WS7-30), with the exception of the $\lambda = 375$ nm photoionization laser which is free-running. The $\lambda = 729$ nm light is generated by a cw Titanium-Sapphire laser (M-Squared SolsTiS), which is locked to a high-finesse reference cavity (Stable Laser Systems). We measure T_2 decay times on the optical quadrupole transition of over 20 ms at present, such that decoherence on this transition negligibly affects the results presented in this work.

Neutral Ca atoms are supplied to the 4 K chamber via a resistively heated oven mounted in the room-temperature vacuum chamber. The $\lambda = 422$ nm photoionization beam, 729 nm qubit beam, and 854 and 866 nm repump beams are delivered through integrated optics, along with both the 397 nm SW and RW EIT $\hat{\boldsymbol{\pi}}$-polarized cooling beams.

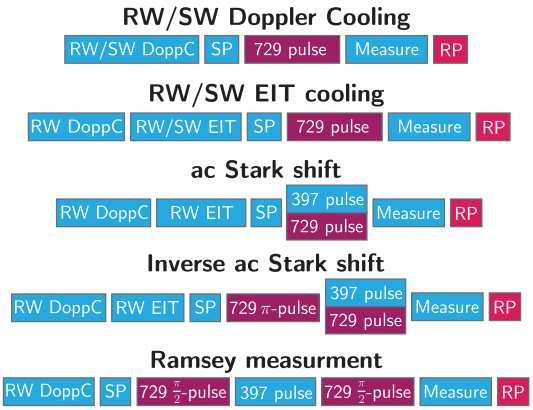


FIG. 8. Experiment sequences used for various measurements. SP and RP stand for state prep and repump respectively.

We employ a free-space optical path for a $\lambda = 397$ nm beam used for both RW Doppler cooling and qubit state readout; the $\hat{\boldsymbol{\sigma}}_+$ beam used for state-preparation and as the EIT pump beam; and the 375 nm photoionization beam. Although $\lambda = 375$ nm waveguides are present on the chip, this photoionization beam is delivered in free space due to the power required and insertion losses in the present device. A custom fiber feedthrough, similar to that described in Refs. [18,70], is used to route fibers into the vacuum chamber and to the VGA attached to the chip.

Experiment sequences used for various measurements in this work are shown in Fig. 8, with the wavelengths and pulse times detailed in Table IV.

Each experiment sequence begins after the previous sequence's readout. Phonon number excitation at the beginning of each shot due to scattering during the preceeding readout can be upper bounded by $\Delta\bar{n} = \eta_0^2 \Gamma t_{\text{read}}/2$. For our axial mode's $\eta_0 = 0.164$ and given our measurement duration $t_{\text{read}} = 250$ μs, $\Delta\bar{n} \approx 450$. Thus, we estimate the axial phonon number to be of order ∼100 before Doppler cooling as we use a close-to-saturation readout pulse.

TABLE IV. Details of the pulses employed in the sequences shown in Fig. 8. Here, FS, RW, SW stand for free-space, integrated RW coupler, and integrated SW coupler beam delivery, respectively. All instances of the "729 pulse" in Fig. 8 correspond to $\lambda = 729$ nm light sent through the integrated coupler.

	Pulse time (μs)	397 nm	866 nm	854 nm
RW DoppC	1500	FS	✓	
SW DoppC	700	SW	✓	
RW EIT	500	FS $\hat{\boldsymbol{\sigma}}_+$ and RW	✓	
SW EIT	150–200	FS $\hat{\boldsymbol{\sigma}}_+$ and SW	✓	
SP	2–5	FS $\hat{\boldsymbol{\sigma}}_+$	✓	✓
Measure	250	FS	✓	
397 pulse	Varying	SW or FS $\hat{\boldsymbol{\sigma}}_+$		
Repump	5		✓	✓

We utilize voltage sets applied to the dc electrodes of the trap to control axial confinement, displacements along radial directions for micromotion-compensation, radial mode orientation, and axial displacement within the SW. These voltages are calculated following the methods in Ref. [71] based on simulations of the trap geometry in Nullspace ES [72], and applied via an open-source DAC (Fastino). Radial confinement is provided by an rf signal generator (Rigol DSG800), impedance-matched to the trap with a lumped-element resonator circuit [73].

Stray dc fields are compensated using sinusoidal modulation of the pseudopotential in a "tickle" technique [74], probing parametric driving of the secular motion as an indication of displacement of the ion from the rf null. Stray fields are compensated with the voltage sets described above. Since the SW has an intensity profile that varies significantly along the horizontal rf micromotion direction ($\hat{y}$), accurate micromotion minimization via stray-field compensation is critical for ion positioning at the node.

For determination of Ω_p parameters that induces the target δ_{EIT} for both RW and EIT cooling, we use the ac Stark shift sequence in Fig. 8 to measure the ac Stark shift of the EIT pump beam on $|4S_{1/2}, m_j = -1/2\rangle$. A Ramsey measurement is used to quantify the small ac Stark shift of the $|4S_{1/2}, m_j = +1/2\rangle$ state induced by impurities in the pump beam. These two results are used to infer the $\hat{\boldsymbol{\sigma}}_+$ pump beam's purity and the associated limit to cooling, detailed in Appendix G. Figure 9 shows examples of the $\lambda = 729$ nm sideband spectroscopy after RW or SW EIT cooling sequences that are used to extract the phonon number following optimized cooling.

We measure compensation position drifts of a few nanometers per minute when light is sent through the integrated SW gratings couplers, but observe that these photo-induced stray fields generally relax back to their initial values over several hours (see details on observed

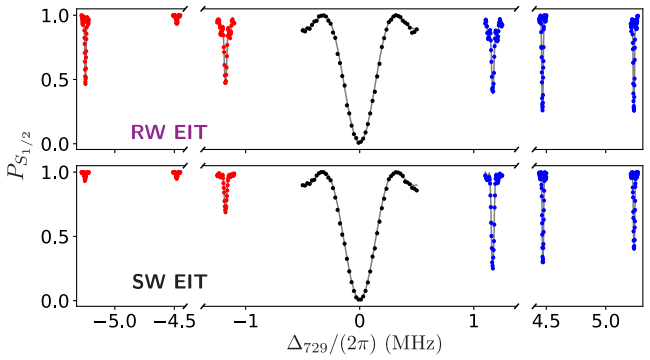


FIG. 9. Sideband spectroscopy after RW (top) and SW (bottom) EIT cooling. Measurements are taken with pulse times of 2.8, 30, and 60 μs for the carrier, axial sidebands, and radial sidebands, respectively. Imbalance in RSB and BSB amplitudes is used to infer $\bar{n}$ values reported in Fig. 6 [44]. Error bars indicate 1σ uncertainty.

drifts in Appendix I). Compensation fields remain approximately stable (within a few percent) over weeks of normal operation. Conductive ITO shielding of the exposed dielectric windows likely contribute to this stability in the presence of the various integrated blue and UV beams; however a more rigorous study is needed to fully understand the effect of ITO in this context.

APPENDIX E: MOTIONAL MODE ORIENTATIONS AND COOLING COEFFICIENTS

To allow simultaneous cooling and probing of R_1 and R_2, we apply voltage sets to the trap's dc electrodes that allow for rotations of the radial mode orientations [71]. We measure the radial modes' orientation from their coupling strength to the $\lambda = 729$ nm beam, whose emission angle is $\theta = 34°$ to the trap surface normal. In Fig. 10, we fit the carrier Rabi oscillations to

$$P_{\downarrow}(t) = 1 - \sum_{n=0}^{\infty} P(n)\sin^2\left(\frac{\Omega_0}{2}(1 - n(\eta_0 \sin\theta)^2 t\right) \quad \text{(E1)}$$

to extract $\Omega_0 = 0.628(2)\ \mu s^{-1}$. BSB Rabi oscillations are fit to

$$P_{\downarrow}(t) = 1 - \sum_{n=0}^{\infty} P(n)\sin^2\left(\frac{\Omega_0}{2}\eta_0 \cos\theta\cos\phi\sqrt{n+1}t\right), \quad \text{(E2)}$$

where $P(n) = \frac{\bar{n}^n}{(\bar{n}+1)^{n+1}}$ are the thermal-state populations and $\eta_0 = \frac{2\pi}{\lambda}\sqrt{\hbar/(2m\omega_m)}$ the Lamb-Dicke parameter for wavelength λ, ion mass m, motional mode frequency ω_m. These fits allow us to extract the radial mode rotation angles from the trap normal of $|\phi| = 51(2)°$ and $49(1)°$ for modes R_1 and R_2 respectively.

The result is approximately consistent with both R_1 and R_2 being rotated 45° counterclockwise with respect to the $\hat{z}$ and $\hat{y}$ axes respectively. As a result, for our analysis we take normal vectors associated with the modes to be $\hat{\boldsymbol{n}}_{R1} = \frac{1}{\sqrt{2}}(-\hat{y} + \hat{z})$, $\hat{\boldsymbol{n}}_{R2} = \frac{1}{\sqrt{2}}(\hat{y} + \hat{z})$.

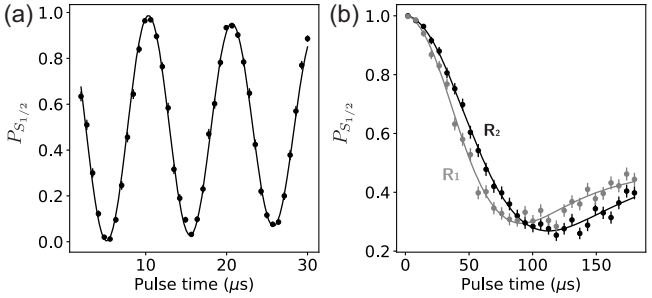


FIG. 10. (a) Carrier and (b) BSB flopping with the same input power of $\lambda = 729$ nm light. We performed the RW Doppler cooling sequence shown in Fig. 8 before the flopping. Error bars in both plots indicate 1σ standard errors from projection noise.

TABLE V. (left) EIT cooling coefficients κ, for the RW configuration: $|\hat{\boldsymbol{n}} \cdot (\boldsymbol{k}_p - \boldsymbol{k}_{RW})/k_0|$ and the SW configuration: $|\hat{\boldsymbol{n}} \cdot (\boldsymbol{k}_{SW1} - \boldsymbol{k}_{SW2})/k_0|$. Motional mode unit vectors for each mode are $\hat{\boldsymbol{n}}_{ax} = (1,0,0)$, $\hat{\boldsymbol{n}}_{R1} = (0, -\frac{1}{\sqrt{2}}, \frac{1}{\sqrt{2}})$, $\hat{\boldsymbol{n}}_{R2} = (0, \frac{1}{\sqrt{2}}, \frac{1}{\sqrt{2}})$, and $\boldsymbol{k} = k_0(\sin\theta\cos\phi, \sin\theta\sin\phi, \cos\theta)$, according to the axes defined in Fig. 2(c). (right) Propagation angles for the involved EIT beams.

	RW κ	SW κ
Axial	1.425	0.612
R_1	0.511	0.433
R_2	0.196	0.433

	Pump	RW	SW1	SW2
θ	90°	60°	60°	60°
ϕ	45°	124°	−45°	135°

For both RW and SW EIT cooling, W_c is proportional to $\kappa^2\eta_0^2\Omega_c^2$ for low cooling beam Rabi frequency Ω_c. κ denotes a "cooling coefficient" that accounts for the motional mode's normal vector relative to the axis cooled, defined by the relevant $\boldsymbol{k}$-vectors. These κ values for both RW and SW EIT cooling of each motional mode are defined and listed in Table V; given our mode and beam orientations, SW EIT cooling acts on all modes, whereas RW EIT would cool the R_1 and axial modes, with much reduced coupling to the R_2 mode.

APPENDIX F: AC STARK SHIFT MOTIONAL-STATE DEPENDENCE

To profile the $\lambda = 397$ nm SW using the ion as a high-resolution probe, we used the ac Stark shift sequence illustrated in Fig. 8. After cooling during each experiment sequence, the $\hat{\boldsymbol{\sigma}}_+$ beam is tuned near to resonance with the $|4S_{1/2}\rangle \leftrightarrow |4P_{1/2}\rangle$ transition to optically pump population into $|4S_{1/2}, m_j = +1/2\rangle$. Then, we measure the spatially dependent ac Stark shift δ through spectroscopy on the $|4S_{1/2}, m_j = +1/2\rangle \leftrightarrow |3D_{5/2}, m_j = +1/2\rangle$ transition while sending $\lambda = 397$ nm light detuned $\Delta = -1$ GHz from the $S_{1/2} \leftrightarrow P_{1/2}$ transition through the SW channel. In the experiment, we use a fiber polarization controller to adjust the input polarization such that $\lambda = 397$ light couples into the waveguide's quasi-TE mode and emits with approximately $\hat{\boldsymbol{\pi}}$-polarization.

The ion's secular motion within the SW profile affects the measured ac Stark shift, reducing the contrast between the maximum and minimum ac Stark shift. The ideal TE-polarized SW in Fig. 11 has

$$\boldsymbol{E}(\boldsymbol{r}, \boldsymbol{t}) = \hat{\boldsymbol{n}} E_0 \sin(k_x x + k_y y + \varphi)\exp[i(k_z z - \omega_L t)]$$

with $\hat{\boldsymbol{n}} = (\hat{x} + \hat{y})/\sqrt{2}$, $k_x = k_0 \sin\theta\cos\phi$, $k_y = k_0 \sin\theta\sin\phi$, $k_z = k_0\cos\theta$, and $\theta = 60°$ and $\phi = 45°$ (Table V).

Because the SW is predominantly $\hat{\boldsymbol{\pi}}$-polarized and the laser detuning Δ in our Stark shift measurements satisfies

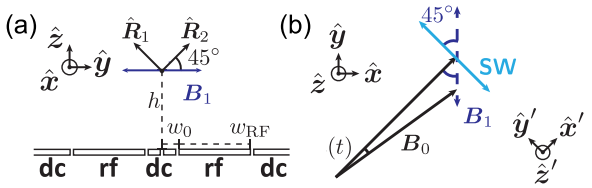


FIG. 11. Geometric considerations relevant to mode orientations and oscillating magnetic fields induced by trap rf currents. (a) Side view of the ion on top of the trap surface. The asymmetric voltage sets, applied on the dc electrodes, rotate the R_1 and R_2 modes 45° clockwise. (b) Rf current charging and discharging the rf electrodes flows along the trap axis $\hat{\boldsymbol{x}}$, resulting in an oscillating magnetic field $\boldsymbol{B}_1$ along $\hat{\boldsymbol{y}}$ at ion's position. To describe quantization axis oscillations, we define a coordinate system with $\hat{\boldsymbol{x}}'$ aligned with the static quantizing magnetic field $\boldsymbol{B}_0$ generated by the permanent magnets.

$\Gamma \ll \Delta \ll \omega_{f,P_{1/2}}$ with $\omega_{f,P}$ the $4P$ levels' fine structure splitting, we approximate the ac Stark shift on $|g\rangle \equiv |4S_{1/2}, m_j = +1/2\rangle$ in terms of its coupling simply to $|e\rangle \equiv |4P_{1/2}, m_j = +1/2\rangle$.

In a frame rotating with laser frequency ω_L and after the usual optical rotating wave approximation, the dipole interaction strength is $\langle e|\tilde{V}_{\text{dip}}|g\rangle = \frac{\Omega(\tilde{\boldsymbol{r}})}{2} = \frac{q\boldsymbol{E}(\tilde{\boldsymbol{r}})\cdot\boldsymbol{d}_{eg}}{2}$, with dipole matrix element $\boldsymbol{d}_{eg}$ (in this section we label operators with tildes). The resulting ac Stark shift on $|4S_{1/2}, m_j = +1/2\rangle$ for large laser detuning $|\Delta|$ is

$$\delta \equiv \left\langle \frac{|\Omega(\tilde{\boldsymbol{r}})|^2}{4\Delta} \right\rangle \tag{F1}$$

with $\tilde{\boldsymbol{r}}$ the ion's position operator and the expectation value $\langle\cdot\rangle$ corresponding to expectation over the motional states of the ion in the spatially varying profile.

To leading orders in the LD parameters of all motional modes, from Eq. (F1) we find for the ac Stark shifts at the node and antinode:

$$\delta_{\text{n}} = \frac{|\Omega_0|^2}{4\Delta}(k_x^2\langle\tilde{x}^2\rangle + k_y^2\langle\tilde{y}^2\rangle) = \frac{|\Omega_0|^2}{4\Delta}\mu$$
$$\delta_{\text{an}} = \frac{|\Omega_0|^2}{4\Delta}(1 - k_x^2\langle\tilde{x}^2\rangle - k_y^2\langle\tilde{y}^2\rangle) = \frac{|\Omega_0|^2}{4\Delta}(1-\mu)$$

where

$$\mu \equiv \eta_{\text{ax}}^2(2\bar{n}_{\text{ax}} + 1) + \sum_{i=1,2}\eta_{R_i}^2(2\bar{n}_{R_i} + 1). \tag{F2}$$

Given the motional modes' orientations as discussed previously, $\tilde{x} = a_{0\text{ax}}(\tilde{a}_{\text{ax}} + \tilde{a}_{\text{ax}}^\dagger)$ and $\tilde{y} = \frac{1}{\sqrt{2}}(a_{0R_1}(\tilde{a}_{R_1} + \tilde{a}_{R_1}^\dagger) - a_{0R_2}(\tilde{a}_{R_2} + \tilde{a}_{R_2}^\dagger))$ are the corresponding position operators of the ion. Here $a_{0j} = \sqrt{\frac{\hbar}{2m\omega_j}}$ for mode j of frequency ω_j; η_j is the corresponding Lamb Dicke parameter $\kappa\eta_o$, and $\bar{n}_j$ is the expectation phonon number for $j \in \{\text{ax}, R_1, R_2\}$. Given the wavepacket extent's influence on the ac Stark shifts, to maximize extinction ratio $\gamma = \delta_{\text{an}}/\delta_{\text{n}}$ and thereby most accurately bound the *optical* extinction via this ac Stark shift profiling, we apply a burst of RW EIT cooling optimized to cool the axial mode. This results in $\bar{n}$ of 0.53(8), 6.0(8), and 3.6(4) for the axial, R_1, and R_2 modes respectively. This corresponds to $\mu = 0.047$, which would give an extinction ratio limited by motional occupancies of $\gamma_0 \approx 20$.

The difference between γ and γ_0 may be due to positional fluctuations in the equilibrium trap position resulting from electric field noise and drift [44], on timescales shorter than those over which we average (of order multiple seconds) to measure ac Stark shifts. These fluctuations are expected to be dominant along the axial direction, which has the lowest trap frequency. Such fluctuations result in ac Stark shifts at the SW node and antinode of $\delta_{\text{n}} = \frac{|\Omega_0|^2}{4\Delta}(\mu + \chi)$ and $\delta_{\text{an}} = \frac{|\Omega_0|^2}{4\Delta}(1 - \mu - \chi)$, where $\chi \equiv k_x^2\langle\delta_x^2\rangle$, where $\langle\delta_x^2\rangle$ is the classical mean squared displacement of the equilibrium trap position. From the known μ due to secular mode occupancy and our measured extinction γ, we estimate $\chi \approx 0.037$. Considering the emission angle θ and SW's angle with respect to the axial direction ϕ, this suggests an axial rms variation $\sqrt{\langle\delta_x^2\rangle} = \sqrt{\chi}/(k_0 \sin\theta\cos\phi) = 19.8$ nm. In simulations, we model the effect of the resulting residual field sampled by the ion at the node by including additional carrier coupling with amplitude $\Omega_{\text{res}} = \Omega_0\sqrt{\chi}/2$.

We roughly estimate the plausibility of E-field noise as the origin of our observed extinction by extrapolating the E-field noise magnitude measured at the secular motional frequencies. The axial mode at $\omega_{\text{ax}} = 1.18$ MHz has a heating rate $\dot{\bar{n}} = 3.9(3) \times 10^3$ s^{-1}, and the relative heating rate for the R_1 mode (Fig. 14) supports roughly $S(\nu) \propto \nu^{-2}$ scaling [75]. We thus suppose that the power spectral density of the electric field noise can be written over an appropriate frequency range as

$$S(\nu) = \frac{4mh\omega_{\text{ax}}}{q^2}\frac{\omega_{\text{ax}}^2}{\nu^2}\dot{\bar{n}}. \tag{F3}$$

We find an rms displacement from E-field noise $q\sqrt{\int_{\omega_{\text{lo}}}^{\infty} S(\nu)d\nu}/(m\omega_{\text{ax}}^2)$ of approximately 20 nm, consistent with the ac Stark shift observations, if we extrapolate over frequency to $\omega_{\text{lo}} \sim 1$ kHz (each ac Stark shift is measured averaged over timescales of multiple seconds). Though we do not know the low-frequency scaling of $S(\nu)$, this indicates the potential plausibility of E-field fluctuation as the origin of the limited extinction, with an effective cutoff of order ~1 kHz roughly consistent with some previous estimates [76]. Measurements of E-field noise near ion traps at frequencies well below the secular frequencies would be valuable to better understand this

behavior, particularly important in contexts requiring precise positioning of ions with respect to control fields.

We note that the above is an upper bound on possible positional fluctuations, as it neglects other potential contributors to imperfect extinction. Quasi-TM polarization components of the waveguide modes feeding the SW couplers, and uneven power delivery from the two SW coupler could also worsen the extinction ratio, but are expected to be negligible in our experiment. After optimizing for quasi-TE polarization, we consistently measure the same extinction ratio, suggesting an insignificant TM component. Through optical measurements utilizing a camera focused on different $\hat{z}$ positions, we also measure the beam power emitted from the two SW couplers separately on the same device used in the ion trap experiment. The power emitted by the two SW couplers was found to be less than 4% different, which would result in $< 0.1\%$ fractional intensity at the SW nodes.

APPENDIX G: $\hat{\sigma}_+$ BEAM PURITY AND TRAP RF-INDUCED B-FIELD OSCILLATIONS

A significant limitation to final phonon number is due to polarization impurity of the $\hat{\boldsymbol{\sigma}}_+$ beam due to magnetic field oscillations associated with the rf currents flowing in the trap [48]. As illustrated in Fig. 11(b), the resulting oscillating magnetic field $\boldsymbol{B}_1$ points along a direction different than that of our static quantizing field $\boldsymbol{B}_0$, therefore resulting in a time-varying quantization axis.

To quantify the resulting impurity, we measure the ac Stark shifts δ_m and δ_p on $|4S_{1/2}, m_j = -1/2\rangle$ and $|4S_{1/2}, m_j = +1/2\rangle$, respectively, at the same $\hat{\boldsymbol{\sigma}}_+$ beam power. Given the B-field oscillations responsible for polarization impurity in our setup as described below, δ_p arises primarily from $\hat{\boldsymbol{\pi}}$ polarization components. Using the same pump beam frequency as in EIT sequence, $\Delta_m = 120$ MHz blue detuned from the $|4S_{1/2}, m_j = -1/2\rangle \leftrightarrow |4P_{1/2}, m_j = +1/2\rangle$ and $\Delta_p = 95$ MHz from $|4S_{1/2}, m_j = +1/2\rangle \leftrightarrow |4P_{1/2}, m_j = +1/2\rangle$ at $B_0 = 8.9$ G. In Fig. 12(a), the δ_m on the level of MHz is measured using the inverse ac Stark shift method in Fig. 8, where a 729 nm π-pulse transports the population from $|4S_{1/2}, m_j = +1/2\rangle$ to $|3D_{5/2}, m_j = +1/2\rangle$ before measuring the ac Stark shift δ on the $|4S_{1/2}, m_j = -1/2\rangle \leftrightarrow |3D_{5/2}, m_j = +1/2\rangle$ transition. On the other hand, we use the Ramsey measurement in Fig. 8 to measure and minimize δ_p to the level of tens of kHz [15]. By optimizing the orientations of $\lambda/2$ and $\lambda/4$ waveplates in the $\hat{\boldsymbol{\sigma}}_+$ beam path, we achieve $\delta_p/\delta_m = 0.376(3)\%$ in Fig. 12(b). Accounting for the relative dipole coupling matrix elements, we infer a $\hat{\boldsymbol{\sigma}}_+$ beam impurity of

$$\epsilon_{\text{imp}} \equiv P_{\hat{\boldsymbol{\pi}}}/P_{\hat{\boldsymbol{\sigma}}_+} = 2\Delta_p/\Delta_m \cdot \delta_p/\delta_m = 0.595\%,$$

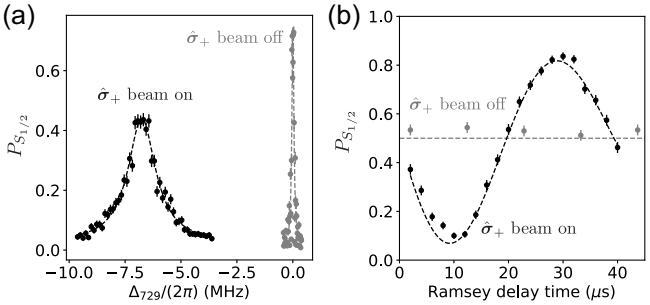


FIG. 12. $\hat{\boldsymbol{\sigma}}_+$-beam intensity and polarization purity diagnostics. (a) Using the inverse ac Stark shift sequence with and without the $\hat{\boldsymbol{\sigma}}_+$-polarized pump beam applied during the 729 nm pulse, spectroscopy on $|4S_{1/2}, m_j = -1/2\rangle \leftrightarrow |3D_{5/2}, m_j = +1/2\rangle$ measures the ac stark shift due to the pump δ_p; such measurements are used to set the pump beam strength for RW and SW EIT, with double the δ for our SW EIT configuration. (b) At the same intensity that resulted in $\delta_p = 2\pi \times 6.75(2)$ MHz in panel (a), a Ramsey sequence on $|4S_{1/2}, m_j = +1/2\rangle \leftrightarrow |3D_{5/2}, m_j = +1/2\rangle$ with and without $\hat{\boldsymbol{\sigma}}_+$ during the Ramsey delay time, indicates $\delta_m = 25.4(2)$ kHz. The second Ramsey pulse is 90° phase-shifted, resulting in $P_{S_{1/2}} = 0.5$ with no frequency shift during the delay time. Error bars in both plots indicate 1σ standard errors from projection noise.

where $P_{\hat{\boldsymbol{\pi}}}$ and $P_{\hat{\boldsymbol{\sigma}}_+}$ are the beam power in $\hat{\boldsymbol{\pi}}$ and $\hat{\boldsymbol{\sigma}}_+$ respectively.

Current flowing through the surface of rf electrode generates an oscillating magnetic field $\boldsymbol{B}_1(t) = B_1 \sin(\Omega_{\text{RF}} t)\hat{\boldsymbol{y}}$, in addition to the stable magnetic field $\boldsymbol{B}_0$ from mounted permanent magnets 45° along the trap axis. Assuming $B_0 \gg B_1$, in a new coordinate system with $\hat{\boldsymbol{x}}'$ aligned with $\boldsymbol{B}_0$ shown in Fig. 11, we have the total magnetic field and the corresponding polarization vectors

$$\begin{aligned}
\boldsymbol{B}(t) &\approx B_0(\cos a(t)\hat{\boldsymbol{x}}' + \sin a(t)\hat{\boldsymbol{y}}') \\
\hat{\boldsymbol{\pi}}(t) &= \cos a(t)\hat{\boldsymbol{x}}' + \sin a(t)\hat{\boldsymbol{y}}' \\
\hat{\boldsymbol{\sigma}}_\pm(t) &= \frac{1}{\sqrt{2}}(-\sin a(t)\hat{\boldsymbol{x}}' + \cos a(t)\hat{\boldsymbol{y}}' \pm i\hat{\boldsymbol{z}}')
\end{aligned}$$

with $a(t) = a\sin(\Omega_{\text{RF}} t) = B_1/(\sqrt{2}B_0)\sin(\Omega_{\text{RF}} t)$.

For a pure $\hat{\boldsymbol{\sigma}}_+$ beam along $\boldsymbol{B}_0$ with $\boldsymbol{E} = E_0/\sqrt{2}(\hat{\boldsymbol{y}}' + i\hat{\boldsymbol{z}}')$ and power P_0, its projections on the polarization components defined with respect to the direction of $\boldsymbol{B}$ are

$$\begin{aligned}
\boldsymbol{E}\cdot\hat{\boldsymbol{\pi}}(t) &= \frac{E_0}{\sqrt{2}}\sin a(t) \approx \frac{E_0}{\sqrt{2}}a(t) \\
\boldsymbol{E}\cdot\hat{\boldsymbol{\sigma}}_+^*(t) &= \frac{E_0}{2}(\cos a(t) + 1) \approx E_0\left(1 - \frac{a(t)^2}{4}\right) \\
\boldsymbol{E}\cdot\hat{\boldsymbol{\sigma}}_-^*(t) &= \frac{E_0}{2}(\cos a(t) - 1) \approx -E_0\frac{a(t)^2}{4}.
\end{aligned}$$

With averaged power

$$P_{\hat{\boldsymbol{\pi}}} \propto \overline{(\boldsymbol{E}\cdot\hat{\boldsymbol{\pi}}(t))^2} = \frac{P_0}{2}\overline{a(t)^2} = P_0\frac{a^2}{4}$$
$$P_{\hat{\boldsymbol{\sigma}}_+} \propto \overline{(\boldsymbol{E}\cdot\hat{\boldsymbol{\sigma}}_+^*(t))^2} \approx P_0\left(1-\frac{\overline{a(t)^2}}{2}\right) = P_0\left(1-\frac{a^2}{4}\right)$$
$$P_{\hat{\boldsymbol{\sigma}}_-} \propto \overline{(\boldsymbol{E}\cdot\hat{\boldsymbol{\sigma}}_-^*(t))^2} = P_0\times\mathcal{O}(a^4)\approx 0,$$

where the bars over quantities indicate a time average. From these expressions we find that an oscillating field amplitude of $B_1 = 1.94$ G would fully explain the ϵ_{imp} observed above.

We estimate B_1 due to the current $I_{\text{rf}}(t) = I_0\sin(\Omega_{\text{rf}}t)$ flowing along the rf electrodes. Considering the boundary condition of zero current at the electrode's end, $I_0 = \frac{1}{2}\Omega_{\text{rf}}C_{\text{trap}}V_{\text{rf}}$ at the trap center, where $\Omega_{\text{rf}} = 2\pi\times 48.4$ MHz, C_{trap} is measured to be 13.5 pF, and the rf voltage amplitude is simulated to be $V_{\text{rf}}\sim 40$ V for 4.4 MHz radial modes, close to our operating condition. Since the electrode dimensions and ion height $h = 50$ μm are much smaller than the wavelength associated with Ω_{rf} MHz, we calculate the quasistatic oscillating B-field amplitude as

$$B_1 = \frac{\mu_0 I_0}{\pi w_{\text{rf}}}\left(\tan^{-1}\left(\frac{w_0+w_{\text{rf}}}{h}\right)-\tan^{-1}\left(\frac{w_0}{h}\right)\right).$$

For our rf electrode width $w_{\text{rf}} = 70$ μm, and the distance from the rf electrode's inner edge to the center axis $w_0 = 27.5$ μm, this yields $B_1 = 2.7$ G. As we measured the trap capacitance after wirebonding it to the carrier PCB with its associated parasitics, this analysis somewhat overestimates the rf current and hence B_1, but the approximate agreement with that inferred from the observed polarization impurity indicates that these field oscillations account for the majority of the polarization impurity observed.

APPENDIX H: LIMITATIONS TO SW EIT COOLING

We carry out fully quantum master equation simulations using the same methods described in our previous work [32], considering the relevant 8-level internal atomic structure and quantized motion, and incorporate experimental parameters and measured nonidealities to understand limitations to the observed EIT cooling performance.

Figure 13 shows the EIT cooling rate W_c and final steady-state phonon number $\bar{n}_{\text{ss}}$ as a function of cooling beam's Rabi frequency Ω_c using the experimental detunings, pump beam amplitude, and motional frequencies. We also include the effects of all key nonidealities, namely the motional mode heating, pump beam polarization impurity, and residual Ω_c carrier coupling at the SW nodes.

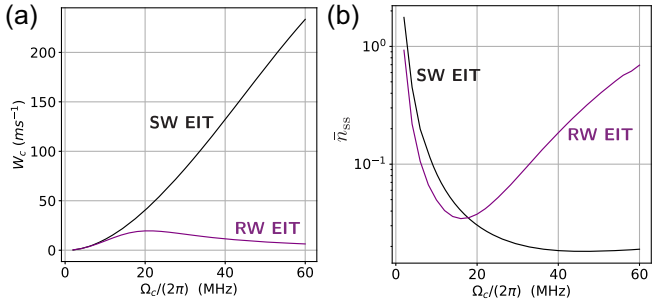


FIG. 13. Simulated EIT cooling comparison incorporating known experimental limitations. (a) Cooling rate and (b) final steady-state phonon number for both SW and RW EIT cooling of R_1 as a function of cooling beam Rabi frequency Ω_c.

With $\Delta_p = 2\pi\times 120$ MHz, we take $\Delta_c = \Delta_p$, $\Omega_p = \sqrt{(\Delta_p+2\omega_{R_1})^2-\Delta_p^2}$ for RW and $\Delta_c = \Delta_p+\omega_{R_1}$, $\Omega_p = \sqrt{8\omega_{R_1}(\Delta_p+2\omega_{R_1})}$ for SW. We extract the cooling rate $W_c = -\dot{\bar{n}}/\bar{n}$ from the time evolution of $\bar{n}(t)$, starting from $\bar{n}(0) = 4$. While simulated RW EIT saturates at $W_c = 20$ ms^{-1} in line with the experimental measured 21(2) ms^{-1}, SW EIT's simulated W_c increases further beyond the measured 57(3) ms^{-1} with lower $\bar{n}_{\text{ss}}$ as Ω_c increases. This suggests that SW EIT can be significantly accelerated further by improving power delivery to the trap, and if positional drifts associated with photo-charging can be mitigated relative to those observed here (see Appendix I). Matching the simulated cooling rates in this figure with those we measured, we estimate $\Omega_c = 2\pi\times 21$ MHz for RW and $\Omega_c = 2\pi\times 24$ MHz for SW; these are used to simulate the final phonon numbers achievable considering the various nonidealities in our experiment.

Table VI shows the simulated final phonon number, achievable at the ideal and different unideal situations: heating rates, residual carrier excitation Ω_{res} from positional fluctuations or imperfect optical extinction, and $\hat{\boldsymbol{\sigma}}_+$ beam impurity ϵ_{imp}. This impurity is the primary limitation preventing cooling down to the 10^{-3} level and can be

TABLE VI. Simulated final phonon numbers $\bar{n}_{\text{ss}}^{\text{RW}}$ and $\bar{n}_{\text{ss}}^{\text{SW}}$ for RW and SW EIT cooling for the R_1 mode. We present these limits under ideal conditions with no technical noise or imperfection, and with contribution of individual nonidealities (heating, residual carrier amplitude at the SW node Ω_{res}, and pump beam polarization impurity ϵ_{imp}), and in the presence of all known nonidealities simultaneously. Simulations use experimental EIT parameters and estimated Ω_c, and include effects of higher-order sidebands in the interaction Hamiltonian.

	Ideal	Heating	Ω_{res}	ϵ_{imp}	All errors
$\bar{n}_{\text{ss}}^{\text{RW}}$	0.03	0.038		0.044	0.052
$\bar{n}_{\text{ss}}^{\text{SW}}$	6.8×10^{-5}	2.8×10^{-3}	1.6×10^{-3}	0.021	0.025

addressed with rf electrode structures that minimize the oscillating magnetic field, or result in oscillating fields only along the direction of the static B-field.

We note that operating at lower Δ_p can reduce optical power required, as the pump beam intensity required for an ideal 3-level system is proportional to $\Omega_p^2 = 8\omega_m(\Delta_p + 2\omega_m)$ for motional frequency ω_m, while the theoretical cooling rate and limit remain unaffected [31]. To compare directly with the results in Ref. [32], we simulate SW EIT cooling at $\Delta_p = 2\Gamma$ and $B = 10$ G, in the ideal case for the 8-level $^{40}Ca^+$ system, targeting $\nu = 2\pi \times 3$ MHz. With the resulting $\Omega_p = 2\pi \times 34.2$ MHz and SW $\Omega_c = 2\pi \times 42$ MHz, the total power $\propto \Omega_p^2 + \frac{\Omega_c^2}{2}$ is comparable to that used in recent work on polarization gradient cooling (PGC) in an integrated platform [27]. Starting from $\bar{n} = 4$, SW EIT cooling for these parameters reaches $\bar{n}_{ss} \approx 0.015$ within about 20 μs. The higher $\bar{n}_{ss}$ compared to that achieved for $\Delta_p = 5\Gamma$ [32] is due to greater deviation from the ideal 3-level system owing to larger off-resonant coupling to $|4P_{1/2}, m_j = -1/2\rangle$. However, the simulated $\bar{n}_{ss}$ and cooling time still suggest that SW EIT's advantage over PGC in terms of cooling limit holds at lower total powers comparable to those used for PGC.

Table VI presents the expected $\bar{n}_{ss}$ limits under our experimental parameters, both in the absence and presence of the known nonidealities. We note that the "ideal" limit predicted here is in fact limited by the Ω_c used in the experiment to achieve high cooling rates, which is only roughly 2× lower than Ω_p and thus perturbs the ideal EIT lineshape. The fundamental limit on phonon number of this scheme is achieved under the low intensity limit; near $\Omega_c = 2\pi \times 5$ MHz and in the absence of technical noise, we simulate that SW EIT results in a steady-state phonon number of $\bar{n}_{ss} = 1 \times 10^{-5}$ for our experimental motional frequency and quantizing field $B_0 = 8.9$ G. This result is insensitive to the quantizing B-field strength as well as whether higher-order interaction terms are included in the simulation, and is in fact limited by sideband couplings in the RW pump beam used our experiments [32].

While our model in the presence of known nonidealities explains the order of magnitude of $\bar{n}_{ss}$ observed experimentally, it still predicts $\bar{n}_{ss}$ approximately 2× lower. We expect that this additional factor of two discrepancy may be due to additional intensity-dependent positional deviations during EIT cooling sequences as compared to the ac stark shift measurements used to estimate these displacements, as well as uncertainties in our polarization impurity measurement. We have additionally considered the effect of relative phase fluctuations between the pump and cooling beams; modeled as Markovian noise, we find that relative linewidths of order 1 MHz would be required to explain this factor of two in final $\bar{n}_{ss}$. This is far in excess of expected levels from acoustic noise and vibrations on the differential fiber paths these beams take prior to the device, but effect of phase fluctuations between the two driving tones may be relevant in experiments reaching significantly lower phonon numbers. Future experiments with suppressed quantization axis oscillations due to trap rf, as well as reduced technical noise, will ultimately be required to validate the significantly lower limits predicted by our model.

We note that when implemented at practical cooling rates (and therefore effective excited state linewidth), even resolved sideband cooling is limited by off-resonant carrier and blue-sideband excitation [30] that are entirely nulled in the SW EIT scheme. Our model thus indicates that if our present technical limitations can be addressed, SW EIT may enable even lower occupancies than achievable with resolved sideband cooling.

APPENDIX I: MOTIONAL HEATING; LIGHT-INDUCED DRIFT

We measure heating rates of secular motional modes of the trapped ion to infer electric field noise at the corresponding frequencies. Figure 14(a) shows measured excitations $\bar{n}$ in both the axial and R_1 modes as a function of wait time after ground-state cooling, indicating heating rates of 3.9(3) and 0.18(1) ms^{-1} respectively. The axial heating rate is consistent with that observed in the previous generation of fabrication [18].

We also characterized slow drifts in ion positioning due to laser-induced charging [77]. We quantify charging by measuring the ion's position drifts relative to the SW, using the ac Stark shift sequence. The ion's position shift is

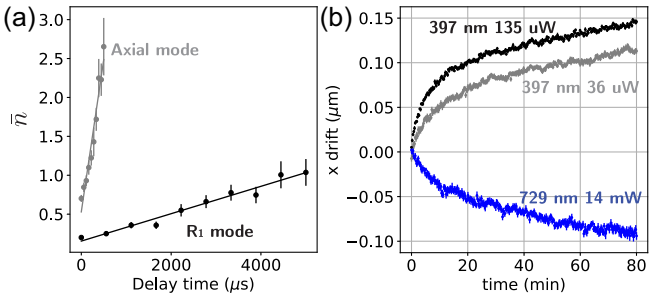


FIG. 14. Electric field noise and drift characterization. (a) Phonon numbers of the axial and R_1 mode as a function of additional delay time after RW EIT cooling of the target mode. We measure the heating rate $\dot{\bar{n}}$ of axial and R_1 mode to be 3.9(3) and 0.18(1) ms^{-1}. (b) Trap position drift along x due to integrated-laser-induced charging. Laser wavelength and input power before the feed-through are labeled in the plot. The drift at each time is inferred from the x-compensation field required to position the ion at a SW node. The three scans were taken on different days spanning over a week; in the multiple hours between scans during with the SW light was off, the trap position relaxed to the same initial value as shown. Error bars in both plots indicate 1σ uncertainty.

inferred from the change in applied dc field along x required to position the ion at the SW node. As shown in Fig. 14(b), the integrated 397 and 729 nm beams shift the ion in different direction along $\hat{\boldsymbol{x}}$, possibly due to couplers' placement. The extent of drift in response to 397 nm light shows a modest power-dependence, while the comparable response to the 729 nm light for drastically higher powers suggests much stronger response to the UV photons. In both cases, upon starting the experimental sequences the ion experiences a rapid drift of 10 s of nm that evolves into a slower constant drift. Between scans and over multiple hours, the trap position relaxed to nearly the same initial value, giving the same x compensation at the target SW node at the beginning of each scan in Fig. 14, suggesting a reversible and reproducible laser-induced charging process. The observed drifts are comparable to those reported against a phase-stable polarization gradient in Ref. [28]. In our experiments, data were taken generally in the limit where pulse sequences had been running for multiple minutes, such that ion positioning was stable to within ∼10 nm. For profiling and cooling experiments, we operated with up to 400 μW incident in fiber before the feedthrough supplying the $\lambda = 397$ nm SW path.

The slow trap location drifts particularly in response to UV light in the waveguide channel may suggest imperfect shielding by the ITO layer. The present 20-nm-thick ITO films exhibited sheet resistances of approximately 400 Ω/square at room temperature, significantly higher than those of optimized films at this thickness. Influence of ITO film quality or surface preparation on the observed drifts would be an interesting and important subject for future study, as well as the relative performance of ITO vs other transparent conductors in this regard [78].

[1] C. D. Bruzewicz, J. Chiaverini, R. McConnell, and J. M. Sage, *Trapped-ion quantum computing: Progress and challenges*, Appl. Phys. Rev. **6**, 021314 (2019).

[2] D. Kielpinski, C. Monroe, and D. J. Wineland, *Architecture for a large-scale ion-trap quantum computer*, Nature (London) **417**, 709 (2002).

[3] J. P. Home, D. Hanneke, J. D. Jost, J. M. Amini, D. Leibfried, and D. J. Wineland, *Complete methods set for scalable ion trap quantum information processing*, Science **325**, 1227 (2009).

[4] J. M. Pino, J. M. Dreiling, C. Figgatt, J. P. Gaebler, S. A. Moses, M. Allman, C. Baldwin, M. Foss-Feig, D. Hayes, K. Mayer *et al.*, *Demonstration of the trapped-ion quantum CCD computer architecture*, Nature (London) **592**, 209 (2021).

[5] R. Bowler, J. Gaebler, Y. Lin, T. R. Tan, D. Hanneke, J. D. Jost, J. P. Home, D. Leibfried, and D. J. Wineland, *Coherent diabatic ion transport and separation in a multizone trap array*, Phys. Rev. Lett. **109**, 080502 (2012).

[6] M. W. van Mourik, E. A. Martinez, L. Gerster, P. Hrmo, T. Monz, P. Schindler, and R. Blatt, *Coherent rotations of qubits within a surface ion-trap quantum computer*, Phys. Rev. A **102**, 022611 (2020).

[7] W. C. Burton, B. Estey, I. M. Hoffman, A. R. Perry, C. Volin, and G. Price, *Transport of multispecies ion crystals through a junction in a radio-frequency Paul trap*, Phys. Rev. Lett. **130**, 173202 (2023).

[8] M. Brownnutt, M. Kumph, P. Rabl, and R. Blatt, *Ion-trap measurements of electric-field noise near surfaces*, Rev. Mod. Phys. **87**, 1419 (2015).

[9] A. Ransford, M. Allman, J. Arkinstall, J. Campora III, S. F. Cooper, R. D. Delaney, J. M. Dreiling, B. Estey, C. Figgatt, A. Hall *et al.*, *Helios: A 98-qubit trapped-ion quantum computer*, arXiv:2511.05465.

[10] C. Monroe, D. M. Meekhof, B. E. King, S. R. Jefferts, W. M. Itano, D. J. Wineland, and P. Gould, *Resolved-sideband Raman cooling of a bound atom to the 3D zero-point energy*, Phys. Rev. Lett. **75**, 4011 (1995).

[11] C. J. Ballance, *High-Fidelity Quantum Logic in Ca+* (Springer, New York, 2017).

[12] S. Ejtemaee and P. C. Haljan, *3D sisyphus cooling of trapped ions*, Phys. Rev. Lett. **119**, 043001 (2017).

[13] M. K. Joshi, A. Fabre, C. Maier, T. Brydges, D. Kiesenhofer, H. Hainzer, R. Blatt, and C. F. Roos, *Polarization-gradient cooling of 1D and 2D ion coulomb crystals*, New J. Phys. **22**, 103013 (2020).

[14] C. F. Roos, D. Leibfried, A. Mundt, F. Schmidt-Kaler, J. Eschner, and R. Blatt, *Experimental demonstration of ground state laser cooling with electromagnetically induced transparency*, Phys. Rev. Lett. **85**, 5547 (2000).

[15] R. Lechner, C. Maier, C. Hempel, P. Jurcevic, B. P. Lanyon, T. Monz, M. Brownnutt, R. Blatt, and C. F. Roos, *Electromagnetically-induced-transparency ground-state cooling of long ion strings*, Phys. Rev. A **93**, 053401 (2016).

[16] K. K. Mehta, C. D. Bruzewicz, R. McConnell, R. J. Ram, J. M. Sage, and J. Chiaverini, *Integrated optical addressing of an ion qubit*, Nat. Nanotechnol. **11**, 1066 (2016).

[17] R. J. Niffenegger, J. Stuart, C. Sorace-Agaskar, D. Kharas, S. Bramhavar, C. D. Bruzewicz, W. Loh, R. T. Maxson, R. McConnell, D. Reens *et al.*, *Integrated multi-wavelength control of an ion qubit*, Nature (London) **586**, 538 (2020).

[18] K. K. Mehta, C. Zhang, M. Malinowski, T.-L. Nguyen, M. Stadler, and J. P. Home, *Integrated optical multi-ion quantum logic*, Nature (London) **586**, 533 (2020).

[19] M. Ivory, W. J. Setzer, N. Karl, H. McGuinness, C. DeRose, M. Blain, D. Stick, M. Gehl, and L. P. Parazzoli, *Integrated optical addressing of a trapped ytterbium ion*, Phys. Rev. X **11**, 041033 (2021).

[20] G. Moody, V. J. Sorger, D. J. Blumenthal, P. W. Juodawlkis, W. Loh, C. Sorace-Agaskar, A. E. Jones, K. C. Balram, J. C. Matthews, A. Laing *et al.*, *2022 roadmap on integrated quantum photonics*, J. Phys. **4**, 012501 (2022).

[21] J. Kwon, W. J. Setzer, M. Gehl, N. Karl, J. Van Der Wall, R. Law, M. G. Blain, D. Stick, and H. J. McGuinness, *Multi-site integrated optical addressing of trapped ions*, Nat. Commun. **15**, 3709 (2024).

[22] C. Mordini, A. Ricci Vasquez, Y. Motohashi, M. Müller, M. Malinowski, C. Zhang, K. K. Mehta, D. Kienzler, and J. P. Home, *Multizone trapped-ion qubit control in an integrated photonics QCCD device*, Phys. Rev. X **15**, 011040 (2025).

[23] K. K. Mehta, C. Zhang, S. Miller, and J. P. Home, *Towards fast and scalable trapped-ion quantum logic with integrated photonics*, in *Advances in Photonics of Quantum Computing, Memory, and Communication XII* (SPIE, Bellingham, Washington, 2019), Vol. 10933, pp. 24–34.

[24] A. R. Vasquez, C. Mordini, C. Vérnière, M. Stadler, M. Malinowski, C. Zhang, D. Kienzler, K. K. Mehta, and J. P. Home, *Control of an atomic quadrupole transition in a phase-stable standing wave*, Phys. Rev. Lett. **130**, 133201 (2023).

[25] S. Saner, O. Băzăvan, M. Minder, P. Drmota, D. J. Webb, G. Araneda, R. Srinivas, D. M. Lucas, and C. J. Ballance, *Breaking the entangling gate speed limit for trapped-ion qubits using a phase-stable standing wave*, Phys. Rev. Lett. **131**, 220601 (2023).

[26] A. M. Kolhatkar and K. K. Mehta, *Efficient optical configurations for trapped-ion entangling gates*, Phys. Rev. A **113**, 042424 (2026).

[27] E. Clements, F. W. Knollmann, S. Corsetti, Z. Li, A. Hattori, M. Notaros, R. Swint, T. Sneh, M. E. Kim, A. D. Leu, P. Callahan, T. Mahony, G. N. West, C. Sorace-Agaskar, D. Kharas, R. McConnell, C. D. Bruzewicz, I. L. Chuang, J. Notaros, and J. Chiaverini, *Sub-doppler cooling of a trapped ion in a phase-stable polarization gradient*, Phys. Rev. Lett. **136**, 023201 (2026).

[28] S. M. Corsetti, A. Hattori, E. R. Clements, F. W. Knollmann, M. Notaros, R. Swint, T. Sneh, P. T. Callahan, G. N. West, D. Kharas, T. Mahony, C. D. Bruzewicz, C. Sorace-Agaskar, R. McConnell, I. L. Chuang, J. Chiaverini, and J. Notaros, *Integrated-photonics-based systems for polarization-gradient cooling of trapped ions*, Light:Sci. Appl. **15**, 57 (2026).

[29] J. I. Cirac, R. Blatt, P. Zoller, and W. D. Phillips, *Laser cooling of trapped ions in a standing wave*, Phys. Rev. A **46**, 2668 (1992).

[30] D. Leibfried, R. Blatt, C. Monroe, and D. Wineland, *Quantum dynamics of single trapped ions*, Rev. Mod. Phys. **75**, 281 (2003).

[31] S. Zhang, C.-W. Wu, and P.-X. Chen, *Dark-state laser cooling of a trapped ion using standing waves*, Phys. Rev. A **85**, 053420 (2012).

[32] Z. Xing and K. K. Mehta, *Trapped-ion laser cooling in structured light fields*, Phys. Rev. Appl. **24**, 014034 (2025).

[33] D. Leibfried, B. DeMarco, V. Meyer, D. Lucas, M. Barrett, J. Britton, W. M. Itano, B. Jelenković, C. Langer, T. Rosenband *et al.*, *Experimental demonstration of a robust, high-fidelity geometric two ion-qubit phase gate*, Nature (London) **422**, 412 (2003).

[34] M. O. Scully and M. S. Zubairy, *Quantum Optics* (Cambridge University Press, Cambridge, England, 1997).

[35] K. Wörhoff, R. G. Heideman, A. Leinse, and M. Hoekman, *Triplex: a versatile dielectric photonic platform*, Adv. Opt. Technol. **4**, 189 (2015).

[36] G. N. West, W. Loh, D. Kharas, C. Sorace-Agaskar, K. K. Mehta, J. Sage, J. Chiaverini, and R. J. Ram, *Low-loss integrated photonics for the blue and ultraviolet regime*, APL Photonics **4**, 026101 (2019).

[37] C. Sorace-Agaskar, D. Kharas, S. Yegnanarayanan, R. T. Maxson, G. N. West, W. Loh, S. Bramhavar, R. J. Ram, J. Chiaverini, J. Sage *et al.*, *Versatile silicon nitride and alumina integrated photonic platforms for the ultraviolet to short-wave infrared*, IEEE J. Sel. Top. Quantum Electron. **25**, 1 (2019).

[38] S. Garcia-Blanco, W. Hendriks, D. Bonneville, S. Mardani, and M. Dijkstra, *UV integrated photonics in sputter deposited aluminum oxide*, Optica Open (2024).

[39] J. Chiaverini, R. B. Blakestad, J. Britton, J. D. Jost, C. Langer, D. Leibfried, R. Ozeri, and D. J. Wineland, *Surface-electrode architecture for ion-trap quantum information processing*, Quant. Inf. Comput. **5**, 419 (2005).

[40] M. Niedermayr, K. Lakhmanskiy, M. Kumph, S. Partel, J. Edlinger, M. Brownnutt, and R. Blatt, *Cryogenic surface ion trap based on intrinsic silicon*, New J. Phys. **16**, 113068 (2014).

[41] K. K. Mehta, A. M. Eltony, C. D. Bruzewicz, I. L. Chuang, R. J. Ram, J. M. Sage, and J. Chiaverini, *Ion traps fabricated in a CMOS foundry*, Appl. Phys. Lett. **105**, 044103 (2014).

[42] K. K. Mehta and R. J. Ram, *Precise and diffraction-limited waveguide-to-free-space focusing gratings*, Sci. Rep. **7**, 2019 (2017).

[43] A. R. Vasquez, C. Mordini, D. Kienzler, and J. Home, *State-dependent control of the motional modes of trapped ions using an integrated optical lattice*, arXiv:2411.03301.

[44] Q. A. Turchette, B. E. King, D. Leibfried, D. M. Meekhof, C. J. Myatt, M. A. Rowe, C. A. Sackett, C. S. Wood, W. M. Itano, C. Monroe, and D. J. Wineland, *Heating of trapped ions from the quantum ground state*, Phys. Rev. A **61**, 063418 (2000).

[45] J. Eschner, G. Morigi, F. Schmidt-Kaler, and R. Blatt, *Laser cooling of trapped ions*, J. Opt. Soc. Am. B **20**, 1003 (2003).

[46] S. Stenholm, *The semiclassical theory of laser cooling*, Rev. Mod. Phys. **58**, 699 (1986).

[47] M. Malinowski, *Unitary and Dissipative Trapped-Ion Entanglement Using Integrated Optics*, Ph.D. thesis, ETH Zurich, 2021.

[48] M. K. Joshi, M. Guevara-Bertsch, F. Kranzl, R. Blatt, and C. F. Roos, *Characterization of ion-trap-induced ac magnetic fields*, Phys. Rev. A **110**, 063101 (2024).

[49] L. He and M. Li, *On-chip synthesis of circularly polarized emission of light with integrated photonic circuits*, Opt. Lett. **39**, 2553 (2014).

[50] G. Spektor, D. Carlson, Z. Newman, J. L. Skarda, N. Sapra, L. Su, S. Jammi, A. R. Ferdinand, A. Agrawal, J. Vučković *et al.*, *Universal visible emitters in nanoscale integrated photonics*, Optica **10**, 871 (2023).

[51] L. Massai, T. Schatteburg, J. P. Home, and K. K. Mehta, *Pure circularly polarized light emission from waveguide microring resonators*, Appl. Phys. Lett. **121**, 121101 (2022).

[52] V. Natarajan, H. M. Rivy, and K. K. Mehta, *Arrayed vector mode emitters*, in *CLEO: Fundamental Science* (Optica Publishing Group, Washington, D.C., 2024), p. JTu2A–223.

[53] O. Jaramillo, V. Natarajan, H. Mahmud Rivy, J. Tensuan, L. Massai, and K. K. Mehta, HfO_2*-based platform for high-index-contrast visible and UV integrated photonics*, Opt. Lett. **50**, 3165 (2025).

[54] F. W. Knollmann, S. M. Corsetti, E. R. Clements, R. Swint, A. D. Leu, M. E. Kim, P. T. Callahan, D. Kharas, T. Mahony, C. Sorace-Agaskar *et al.*, *Collection of fluorescence from an ion using trap-integrated photonics*, arXiv:2505.01412.

[55] A. Hughes, R. Srinivas, C. Löschnauer, H. Knaack, R. Matt, C. Ballance, M. Malinowski, T. Harty, and R. Sutherland, *Trapped-ion two-qubit gates with > 99.99% fidelity without ground-state cooling*, arXiv:2510.17286.

[56] L. Feng, W. L. Tan, A. De, A. Menon, A. Chu, G. Pagano, and C. Monroe, *Efficient ground-state cooling of large trapped-ion chains with an electromagnetically-induced-transparency tripod scheme*, Phys. Rev. Lett. **125**, 053001 (2020).

[57] C. Huang, C. Wang, H. Zhang, H. Hu, Z. Wang, Z. Mao, S. Li, P. Hou, Y. Wu, Z. Zhou *et al.*, *Electromagnetically induced transparency cooling of high-nuclear-spin ions*, Phys. Rev. Lett. **133**, 113204 (2024).

[58] J. P. Bartolotta, B. Estey, M. Foss-Feig, D. Hayes, and C. N. Gilbreth, *Laser cooling trapped-ion crystal modes beyond the Lamb-Dicke regime*, arXiv:2411.18818.

[59] J. D. Thompson, T. G. Tiecke, A. S. Zibrov, V. Vuletić, and M. D. Lukin, *Coherence and Raman sideband cooling of a single atom in an optical tweezer*, Phys. Rev. Lett. **110**, 133001 (2013).

[60] A. M. Kaufman, B. J. Lester, and C. A. Regal, *Cooling a single atom in an optical tweezer to its quantum ground state*, Phys. Rev. X **2**, 041014 (2012).

[61] A. Jenkins, J. W. Lis, A. Senoo, W. F. McGrew, and A. M. Kaufman, *Ytterbium nuclear-spin qubits in an optical tweezer array*, Phys. Rev. X **12**, 021027 (2022).

[62] C. T. Schmiegelow and F. Schmidt-Kaler, *Light with orbital angular momentum interacting with trapped ions*, Eur. Phys. J. D **66**, 157 (2012).

[63] M. Verde, C. T. Schmiegelow, U. Poschinger, and F. Schmidt-Kaler, *Trapped atoms in spatially-structured vector light fields*, Sci. Rep. **13**, 21283 (2023).

[64] X. Mai, L. Zhang, Q. Yu, J. Zhang, and Y. Lu, *Scalable entangling gates on ion qubits via structured light addressing*, arXiv:2506.19535.

[65] J.-M. Cui, Y. Chen, Y.-F. Zhou, Q. Long, E.-T. An, R. He, Y.-F. Huang, C.-F. Li, and G.-C. Guo, *Transverse polarization gradient entangling gates for trapped-ion quantum computation*, Phys. Rev. Lett. **135**, 260604 (2025).

[66] M. Momenzadeh, K. Sun, Q. Wu, B. You, Y.-L. Tang, H. Häffner, and M. R. Shcherbakov, *Individual trapped-ion addressing with adjoint-optimized multimode photonic circuits*, npj Nanophotonics **3**, 3 (2026).

[67] A. A. Peshkov, E. Jordan, M. Kromrey, K. K. Mehta, T. E. Mehlstäubler, and A. Surzhykov, *Excitation of forbidden electronic transitions in atoms by Hermite–Gaussian modes*, Ann. Phys. (Amsterdam) **535**, 2300204 (2023).

[68] *Data and simulation results used in this paper*, https: //github.com/PQEGroup/swcooling_data.

[69] G. J. Beck, J. P. Home, and K. K. Mehta, *Grating design methodology for tailored free-space beam-forming*, J. Lightwave Technol. **42**, 4939 (2024).

[70] C. Zhang, *Scalable Technologies for Surface-Electrode Ion Traps*, Ph.D. thesis, ETH Zurich, 2021.

[71] D. Allcock, J. Sherman, D. Stacey, A. Burrell, M. Curtis, G. Imreh, N. Linke, D. Szwer, S. Webster, A. Steane *et al.*, *Implementation of a symmetric surface-electrode ion trap with field compensation using a modulated Raman effect*, New J. Phys. **12**, 053026 (2010).

[72] Nullspace ES, https://www.nullspaceinc.com.

[73] D. Gandolfi, M. Niedermayr, M. Kumph, M. Brownnutt, and R. Blatt, *Compact radio-frequency resonator for cryogenic ion traps*, Rev. Sci. Instrum. **83**, 084705 (2012).

[74] Y. Ibaraki, U. Tanaka, and S. Urabe, *Detection of parametric resonance of trapped ions for micromotion compensation*, Appl. Phys. B **105**, 219 (2011).

[75] J. A. Sedlacek, J. Stuart, D. H. Slichter, C. D. Bruzewicz, R. McConnell, J. M. Sage, and J. Chiaverini, *Evidence for multiple mechanisms underlying surface electric-field noise in ion traps*, Phys. Rev. A **98**, 063430 (2018).

[76] I. Talukdar, D. J. Gorman, N. Daniilidis, P. Schindler, S. Ebadi, H. Kaufmann, T. Zhang, and H. Häffner, *Implications of surface noise for the motional coherence of trapped ions*, Phys. Rev. A **93**, 043415 (2016).

[77] S. X. Wang, G. Hao Low, N. S. Lachenmyer, Y. Ge, P. F. Herskind, and I. L. Chuang, *Laser-induced charging of microfabricated ion traps*, J. Appl. Phys. **110**, 104901 (2011).

[78] W. Wang, D. Fomra, A. Agrawal, H. J. Lezec, and J. W. Britton, *Can TCOs transform cavity-QED?*, arXiv:2506.02501.